High Resolution Spectroscopic Observation of the Bound-Free Hyperfine Levels of a Novel Hydride Ion Corresponding to a Fractional Rydberg State of Atomic Hydrogen

R. L. Mills, P. Ray

BlackLight Power, Inc., 493 Old Trenton Road, Cranbury, NJ 08512

From a solution of a Schrödinger-type wave equation with a nonradiative boundary condition based on Maxwell's equations, Mills solves the hydrogen atom, the hydride ion, and predicts corresponding species having fractional principal quantum numbers. Atomic hydrogen may undergo a catalytic reaction with certain atomized elements and ions which singly or multiply ionize at integer multiples of the potential energy of atomic hydrogen, $m \cdot 27.2\ eV$ wherein m is an integer. The reaction involves a nonradiative energy transfer to form a hydrogen atom $H(1/p)$ that is lower in energy than unreacted atomic hydrogen that corresponds to a fractional principal quantum number ($n = \frac{1}{p} = \frac{1}{\text{integer}}$ replaces the well known parameter n = integer in the Rydberg equation for hydrogen excited states). The ionization of Rb^+ and an electron transfer between two K^+ ions (K^+ / K^+) provide a reaction with a net enthalpy of $27.2\ eV$ which serve as catalysts of atomic hydrogen to form $H(1/2)$. Intense extreme ultraviolet (EUV) emission was observed from incandescently heated atomic hydrogen and each of atomized potassium and rubidium ions that generated a plasma called a resonance transfer or rt-plasma at low temperatures (e.g. $\approx 10^3\ K$) and an extraordinary low field strength of about 1-2 V/cm. For further characterization, the width of the 6562 Å Balmer α line was recorded. Significant line broadening of 17 and 9 eV was observed from a rt-plasma of hydrogen with K^+ / K^+ and Rb^+ respectively. These results could not be explained by Stark or thermal broadening or electric field acceleration of charged species since the measured field of the incandescent heater was extremely weak, 1 V/cm, corresponding to a broadening of much less than 1 eV. Rather the source of the excessive line broadening is consistent with that of the observed EUV emission, an energetic reaction caused by a resonance energy transfer between hydrogen atoms and K^+ / K^+ or Rb^+. The catalyst product $H(1/2)$ was predicted to be a highly reactive intermediate which further reacts to form a novel hydride ion $H^-(1/2)$. This hydride ion with a predicted binding energy of $3.0468\ eV$ was observed by high resolution visible spectroscopy as a broad peak at 4070.0 Å with a FWHM of 1.4 Å. From the electron g factor, bound-free hyperfine structure lines of $H^-(1/2)$ were predicted with energies E_{HF} given by $E_{HF} = j^2 3.0056\ X\ 10^{-5} + 3.0575\ eV$ (j is an integer) as an inverse Rydberg-type series that converges at increasing wavelengths and terminates at $3.0575\ eV$—the hydride spin-pairing energy plus the binding energy. The high resolution visible plasma emission spectra in the region of 4000 Å to 4060 Å matched the predicted emission lines for $j = 1$ to $j = 37$.

I. INTRODUCTION

A. Background

J. J. Balmer showed in 1885 that the frequencies for some of the lines observed in the emission spectrum of atomic hydrogen could be expressed with a completely empirical relationship. This approach was later extended by J. R. Rydberg, who showed that all of the spectral lines of atomic hydrogen were given by the equation:

$$\bar{\nu} = R\left(\frac{1}{n_f^2} - \frac{1}{n_i^2}\right) \tag{1}$$

where $R = 109{,}677\ cm^{-1}$, $n_f = 1,2,3,...$, $n_i = 2,3,4,...$, *and* $n_i > n_f$.

Niels Bohr, in 1913, developed a theory for atomic hydrogen that gave the energy levels in agreement with Rydberg's equation. An identical equation, based on a totally different theory for the hydrogen atom, was developed by E. Schrödinger, and independently by W. Heisenberg, in 1926.

$$E_n = -\frac{e^2}{n^2 8\pi\varepsilon_o a_H} = -\frac{13.598\ eV}{n^2} \tag{2a}$$

$$n = 1,2,3,... \tag{2b}$$

where a_H is the Bohr radius for the hydrogen atom ($52.947\ pm$), e is the magnitude of the charge of the electron, and ε_o is the vacuum permittivity.

The excited energy states of atomic hydrogen are given by Eq. (2a) for $n > 1$ in Eq. (2b). The $n = 1$ state is the "ground" state for "pure" photon transitions (the $n = 1$ state can absorb a photon and go to an excited electronic state, but it cannot release a photon and go to a lower-energy electronic state). However, an electron transition from the ground state to a lower-energy state may be possible by a nonradiative energy transfer such as multipole coupling or a resonant collision mechanism. Processes such as hydrogen molecular bond formation that occur without photons and that require collisions are common [1]. Also, some commercial phosphors are based on resonant nonradiative energy transfer involving multipole coupling [2].

We propose that atomic hydrogen may undergo a catalytic reaction with certain atomized elements and ions which singly or multiply ionize

at integer multiples of the potential energy of atomic hydrogen, $m \cdot 27.2\,eV$ wherein m is an integer. The theory and supporting data was given previously [3-37]. The reaction involves a nonradiative energy transfer to form a hydrogen atom that is lower in energy than unreacted atomic hydrogen called a *hydrino* that corresponds to a fractional principal quantum number. That is

$$n = \frac{1}{2}, \frac{1}{3}, \frac{1}{4}, ..., \frac{1}{p}; \quad p \text{ is an integer} \tag{2c}$$

replaces the well known parameter $n = \text{integer}$ in the Rydberg equation for hydrogen excited states. The $n = 1$ state of hydrogen and the $n = \frac{1}{\text{integer}}$ states of hydrogen are nonradiative, but a transition between two nonradiative states is possible via a nonradiative energy transfer, say $n = 1$ to $n = 1/2$. In these cases, during the transition the electron couples to another electron transition, electron transfer reaction, or inelastic scattering reaction which can absorb the exact amount of energy that must be removed from the hydrogen atom to cause the transition. Thus, a catalyst provides a net positive enthalpy of reaction of $m \cdot 27.2\,eV$ (i.e. it absorbs $m \cdot 27.2\,eV$ where m is an integer). Certain atoms or ions serve as catalysts which resonantly accept the nonradiative energy transfer from hydrogen atoms and release the energy to the surroundings to affect electronic transitions to fractional quantum energy levels. As a consequence of the nonradiative energy transfer, the hydrogen atom becomes unstable and emits further energy until it achieves a lower-energy nonradiative state having a principal energy level given by Eqs. (2a) and (2c).

B. rt-plasma

It was reported previously that a new plasma source has been developed that operates by incandescently heating a hydrogen dissociator to provide atomic hydrogen and heats a catalyst such that it becomes gaseous and reacts with the atomic hydrogen to produce a rt-plasma. It was extraordinary, that intense EUV emission was observed by Mills et al. [11, 13-15, 23-24, 26-27] at low temperatures (e.g. $\approx 10^3\,K$) from atomic hydrogen and certain atomized elements or certain gaseous

ions which singly or multiply ionize at integer multiples of the potential energy of atomic hydrogen, $27.2\,eV$ that comprise catalysts. The only pure elements that were observed to emit EUV were those wherein the ionization of t electrons from an atom to a continuum energy level is such that the sum of the ionization energies of the t electrons is approximately

$$m \cdot 27.2\,eV \tag{3}$$

where t and m are each an integer. Alternatively, a catalyst depended on the transfer of t electrons between participating ions such that the transfer of t electrons from one ion to another ion provides a net enthalpy of reaction whereby the sum of the ionization energy of the electron donating ion minus the ionization energy of the electron accepting ion equals approximately $m \cdot 27.2\,eV$.

Since Ar^+ and strontium each ionize at an integer multiple of the potential energy of atomic hydrogen, a discharge with one or more of these species present with hydrogen was anticipated to form a rt-plasma wherein the plasma forms by a resonance transfer mechanism involving the species providing a net enthalpy of a multiple of $27.2\,eV$ and atomic hydrogen.

Mills and Nansteel [11, 16-17, 23] have reported that strontium atoms each ionize at an integer multiple of the potential energy of atomic hydrogen and caused emission. (The enthalpy of ionization of Sr to Sr^{5+} has a net enthalpy of reaction of $188.2\,eV$, which is equivalent to $m=7$.) The emission intensity of the plasma generated by atomic strontium increased significantly with the introduction of argon gas only when Ar^+ emission was observed. Whereas, no emission was observed when chemically similar atoms that do not ionize at integer multiples of the potential energy of atomic hydrogen (sodium, magnesium, or barium) replaced strontium with hydrogen, hydrogen-argon mixtures, or strontium alone.

Mills and Nanstell [16-17, 23] measured the power balance of a gas cell having vaporized strontium and atomized hydrogen from pure hydrogen or argon-hydrogen mixture (77/23%) by integrating the total light output corrected for spectrometer system response and energy over the visible range. Hydrogen control cell experiments were identical except that sodium, magnesium, or barium replaced strontium. In the case of hydrogen-sodium, hydrogen-magnesium, and hydrogen-barium

mixtures, 4000, 7000, and 6500 times the power of the hydrogen-strontium mixture was required, respectively, in order to achieve that same optically measured light output power. With the addition of argon to the hydrogen-strontium plasma, the power required to achieve that same optically measured light output power was reduced by a factor of about two. The power required to maintain a plasma of equivalent optical brightness with strontium atoms present was 8600 and 6300 times less than that required for argon-hydrogen and argon control, respectively. A plasma formed at a cell voltage of about 250 V for hydrogen alone and sodium-hydrogen mixtures, 140-150 V for hydrogen-magnesium and hydrogen-barium mixtures, 224 V for an argon-hydrogen mixture, and 190 V for argon alone; whereas, a plasma formed for hydrogen-strontium mixtures and argon-hydrogen-strontium mixtures at extremely low voltages of about 2 V and 6.6 V, respectively.

It was reported [15] that characteristic emission was observed from a continuum state of Ar^{2+} which confirmed the resonant nonradiative energy transfer of $27.2\,eV$ from atomic hydrogen Ar^{+}. The transfer of $27.2\,eV$ from atomic hydrogen to Ar^{+} in the presence of a electric weak field resulted in its excitation to a continuum state. Then, the energy for the transition from essentially the Ar^{2+} state to the lowest state of Ar^{+} was predicted to give a broad continuum radiation in the region of 456 Å. This broad continuum emission was observed. This emission was dramatically different from that given by an argon microwave plasma wherein the entire Rydberg series of lines of Ar^{+} was observed with a discontinuity of the series at the limit of the ionization energy of Ar^{+} to Ar^{2+}. The observed Ar^{+} continuum in the region of 456 Å confirmed the rt-plasma mechanism of the excessively bright, extraordinarily low voltage discharge. The product hydride ion with Ar^{+} as a reactant was predicted to have a binding energy of $3.05\,eV$ and was observed spectroscopically at 4070 Å [11, 15].

A number of independent experimental observations lead to the conclusion that atomic hydrogen can exist in fractional quantum states that are at lower energies than the traditional "ground" ($n=1$) state. Prior related studies that support the possibility of a novel reaction of atomic hydrogen which produces a chemically generated or assisted plasma (rt-plasma) and produces novel hydride compounds include extreme

ultraviolet (EUV) spectroscopy [8-11, 13-17, 19-20, 23-25], characteristic emission from catalysis and the hydride ion products [11-15], lower-energy hydrogen emission [6, 8, 9-10, 19], plasma formation [11, 13-15, 23-24, 26-27], Balmer α line broadening [9, 11, 16-17, 19-21], elevated electron temperature [9, 20], anomalous plasma afterglow duration [26-27], power generation [9, 11, 16-19, 21-23, 34], and analysis of chemical compounds [28-34]. Furthermore, mobility and spectroscopy data of individual electrons in liquid helium shows direct experimental confirmation that electrons may have fractional principal quantum energy levels [7].

C. Catalysts

a. Potassium Ions

Potassium ions can provide a net enthalpy of a multiple of that of the potential energy of the hydrogen atom. The second ionization energy of potassium is $31.63\,eV$; and K^+ releases $4.34\,eV$ when it is reduced to K. The combination of reactions K^+ to K^{2+} and K^+ to K, then, has a net enthalpy of reaction of $27.28\,eV$, which is equivalent to $m=1$ in Eq. (3).

$$27.28\,eV + K^+ + K^+ + H\left[\frac{a_H}{p}\right] \rightarrow K + K^{2+} + H\left[\frac{a_H}{(p+1)}\right] + [(p+1)^2 - p^2]\,X\,13.6\,eV \qquad (4)$$

$$K + K^{2+} \rightarrow K^+ + K^+ + 27.28\,eV \qquad (5)$$

The overall reaction is

$$H\left[\frac{a_H}{p}\right] \rightarrow H\left[\frac{a_H}{(p+1)}\right] + [(p+1)^2 - p^2]\,X\,13.6\,eV \qquad (6)$$

Alkali metal nitrates are extraordinarily volatile and can be distilled at 350-500 °C [38]. Gaseous potassium ions were provided by heating KNO_3.

b. Potassium atom

An atomic catalytic system involves potassium atoms. The first, second, and third ionization energies of potassium are $4.34066\,eV$, $31.63\,eV$,

45.806 eV, respectively [39]. The triple ionization ($t=3$) reaction of K to K^{3+}, then, has a net enthalpy of reaction of 81.7766 eV, which is equivalent to $m=3$ in Eq. (3).

$$81.7766\ eV + K(m) + H\left[\frac{a_H}{p}\right] \rightarrow K^{3+} + 3e^- + H\left[\frac{a_H}{(p+3)}\right] + [(p+3)^2 - p^2]X13.6\ eV \quad (7)$$

$$K^{3+} + 3e^- \rightarrow K(m) + 81.7766\ eV \quad (8)$$

And, the overall reaction is

$$H\left[\frac{a_H}{p}\right] \rightarrow H\left[\frac{a_H}{(p+3)}\right] + [(p+3)^2 - p^2]X13.6\ eV \quad (9)$$

Vaporized atomic potassium was formed by hydrogen reduction and thermal decomposition of KNO_3.

c. Rubidium ion

Rubidium ions can also provide a net enthalpy of a multiple of that of the potential energy of the hydrogen atom. The second ionization energy of rubidium is 27.28 eV. The reaction Rb^+ to Rb^{2+} has a net enthalpy of reaction of 27.28 eV, which is equivalent to $m=1$ in Eq. (3).

$$27.28\ eV + Rb^+ + H\left[\frac{a_H}{p}\right] \rightarrow Rb^{2+} + e^- + H\left[\frac{a_H}{(p+1)}\right] + [(p+1)^2 - p^2]X13.6\ eV \quad (10)$$

$$Rb^{2+} + e^- \rightarrow Rb^+ + 27.28\ eV \quad (11)$$

The overall reaction is

$$H\left[\frac{a_H}{p}\right] \rightarrow H\left[\frac{a_H}{(p+1)}\right] + [(p+1)^2 - p^2]\ X\ 13.6\ eV \quad (12)$$

$RbNO_3$ was the favored candidate for providing gaseous Rb^+ ions due to its volatility [38].

D. Classical Quantum Theory of the Atom Based on Maxwell's Equations Predicts Hyperfine Levels of Novel Hydride Ions

a. One Electron Atoms

A theory of classical quantum mechanics (CQM), derived from first principles, that successfully applies physical laws on all scales was given previously [3-7]. One-electron atoms include the hydrogen atom, He^{+}, Li^{2+}, Be^{3+}, and so on. The mass-energy and angular momentum of the electron are constant; this requires that the equation of motion of the electron be temporally and spatially harmonic. Thus, the classical wave equation applies and

$$\left[\nabla^2 - \frac{1}{v^2}\frac{\partial^2}{\partial t^2}\right]\rho(r,\theta,\phi,t) = 0 \tag{13}$$

where $\rho(r,\theta,\phi,t)$ is the time dependent charge density function of the electron in time and space. In general, the wave equation has an infinite number of solutions. To arrive at the solution which represents the electron, a suitable boundary condition must be imposed. It is well known from experiments that each single atomic electron of a given isotope radiates to the same stable state. Thus, the physical boundary condition of nonradiation of the bound electron was imposed on the solution of the wave equation for the time dependent charge density function of the electron [3, 5, 7]. The condition for radiation by a moving point charge given by Haus [40] is that its spacetime Fourier transform does possess components that are synchronous with waves traveling at the speed of light. Conversely, it is proposed that the condition for nonradiation by an ensemble of moving point charges that comprises a current density function is

> *For non-radiative states, the current-density function must NOT possess spacetime Fourier components that are synchronous with waves traveling at the speed of light.*

The time, radial, and angular solutions of the wave equation are separable. The motion is time harmonic with frequency ω_n. A constant angular function is a solution to the wave equation. The solution for the

radial function which satisfies the boundary condition is a radial delta function

$$f(r)=\frac{1}{r^2}\delta(r-r_n) \tag{14}$$

which defines a constant charge function on a spherical shell where $r_n = nr_1$. Given time harmonic motion and a radial delta function, the relationship between an allowed radius and the electron wavelength is given by

$$2\pi r_n = \lambda_n \tag{15}$$

Using the observed de Broglie relationship for the electron mass where the coordinates are spherical,

$$\lambda_n = \frac{h}{p_n} = \frac{h}{m_e v_n} \tag{16}$$

and the magnitude of the velocity for *every* point on the spherical shell is

$$v_n = \frac{\hbar}{m_e r_n} \tag{17}$$

The sum of the $\mathbf{L}_i$, the magnitude of the angular momentum of each infinitesimal point of the shell of mass m_i, must be constant. The constant is $\hbar$.

$$\sum|\mathbf{L}_i| = \sum|\mathbf{r}\times m_i\mathbf{v}| = m_e r_n \frac{\hbar}{m_e r_n} = \hbar \tag{18}$$

Thus, an electron is a spinning, two-dimensional spherical surface, called an *electron orbitsphere*, that can exist in a bound state at only specified distances from the nucleus as shown in Figure 1[1]. The corresponding current function shown in Figure 2 which gives rise to the phenomenon of *spin* is derived in the Spin Function section of Ref. 3.

Nonconstant functions are also solutions for the angular functions. To be a harmonic solution of the wave equation in spherical coordinates,

---

[1] Mobility measurements and spectroscopy directly show that electrons may be trapped in superfluid helium as autonomous electron bubbles interloped between helium atoms that have been excluded from the space occupied by the bubble. Electrons bubbles in superfluid helium reveal that the electron is real and that a physical interpretation of the wavefunction is necessary. The electron orbitsphere representation matches the data identically and is also in agreement with scattering experiments, another direct determination of the nature of the electron [7].

these angular functions must be spherical harmonic functions. A zero of the spacetime Fourier transform of the product function of two spherical harmonic angular functions, a time harmonic function, and an unknown radial function is sought. The solution for the radial function which satisfies the boundary condition is also a delta function given by Eq. (14). Thus, bound electrons are described by a charge-density (mass-density) function which is the product of a radial delta function, two angular functions (spherical harmonic functions), and a time harmonic function.

$$\rho(r,\theta,\phi,t) = f(r)A(\theta,\phi,t) = \frac{1}{r^2}\delta(r-r_n)A(\theta,\phi,t); \qquad A(\theta,\phi,t) = Y(\theta,\phi)k(t) \tag{19}$$

In these cases, the spherical harmonic functions correspond to a traveling charge density wave confined to the spherical shell which gives rise to the phenomenon of orbital angular momentum. The orbital functions which modulate the constant "spin" function shown graphically in Figure 3 are given in the "Angular Functions" section of Ref. 3 and 5.

b. Spin Function

The orbitsphere spin function comprises a constant charge density function with moving charge confined to a two-dimensional spherical shell. The current pattern of the orbitsphere spin function comprises an infinite series of correlated orthogonal great circle current loops wherein each point moves time harmonically with angular velocity

$$\omega_n = \frac{\hbar}{m_e r_n^2} \tag{20}$$

The current pattern is generated over the surface by a series of nested rotations of two orthogonal great circle current loops where the coordinate axes rotate with the two orthogonal great circles. Half of the pattern is generated as the z-axis rotates to the negative z-axis during a 1st set of nested rotations. The mirror image, second half of the pattern is generated as the z-axis rotates back to its original direction during a 2nd set of nested rotations.

Points on Great Circle Current Loop One:

$$\begin{bmatrix} x_1 \\ y_1 \\ z_1 \end{bmatrix} = \begin{bmatrix} \cos(\Delta\alpha) & -\sin^2(\Delta\alpha) & -\sin(\Delta\alpha)\cos(\Delta\alpha) \\ 0 & \cos(\Delta\alpha) & -\sin(\Delta\alpha) \\ \sin(\Delta\alpha) & \cos(\Delta\alpha)\sin(\Delta\alpha) & \cos^2(\Delta\alpha) \end{bmatrix} \begin{bmatrix} x_1' \\ y_1' \\ z_1' \end{bmatrix} \qquad (21)$$

and $\Delta\alpha' = -\Delta\alpha$ replaces $\Delta\alpha$ for $\sum_{n=1}^{\frac{\sqrt{2}\pi}{\Delta\alpha}} \Delta\alpha = \sqrt{2}\pi$; $\sum_{n=1}^{\frac{\sqrt{2}\pi}{|\Delta\alpha'|}} |\Delta\alpha'| = \sqrt{2}\pi$

Points on Great Circle Current Loop Two:

$$\begin{bmatrix} x_2 \\ y_2 \\ z_2 \end{bmatrix} = \begin{bmatrix} \cos(\Delta\alpha) & -\sin^2(\Delta\alpha) & -\sin(\Delta\alpha)\cos(\Delta\alpha) \\ 0 & \cos(\Delta\alpha) & -\sin(\Delta\alpha) \\ \sin(\Delta\alpha) & \cos(\Delta\alpha)\sin(\Delta\alpha) & \cos^2(\Delta\alpha) \end{bmatrix} \begin{bmatrix} x_2' \\ y_2' \\ z_2' \end{bmatrix} \qquad (22)$$

and $\Delta\alpha' = -\Delta\alpha$ replaces $\Delta\alpha$ for $\sum_{n=1}^{\frac{\sqrt{2}\pi}{\Delta\alpha}} \Delta\alpha = \sqrt{2}\pi$; $\sum_{n=1}^{\frac{\sqrt{2}\pi}{|\Delta\alpha'|}} |\Delta\alpha'| = \sqrt{2}\pi$

The orbitsphere is given by reiterations of Eqs. (21) and (22). The output given by the non primed coordinates is the input of the next iteration corresponding to each successive nested rotation by the infinitesimal angle where the summation of the rotation about each of the x-axis and the y-axis is $\sum_{n=1}^{\frac{\sqrt{2}\pi}{\Delta\alpha}} \Delta\alpha = \sqrt{2}\pi$ (1st set) and $\sum_{n=1}^{\frac{\sqrt{2}\pi}{|\Delta\alpha'|}} |\Delta\alpha'| = \sqrt{2}\pi$ (2nd set). The current pattern corresponding to great circle current loop one and two shown with 8.49 degree increments of the infinitesimal angular variable $\Delta\alpha(\Delta\alpha')$ of Eqs. (21) and (22) is shown from the perspective of looking along the z-axis in Figure 2. The true orbitsphere current pattern is given as $\Delta\alpha(\Delta\alpha')$ approaches zero. This current pattern gives rise to the phenomenon corresponding to the spin quantum number of the electron.

c. Magnetic Field Equations of the Electron

The orbitsphere is a shell of negative charge current comprising correlated charge motion along great circles. For l = 0, the orbitsphere gives rise to a magnetic moment of 1 Bohr magneton [41].

$$\mu_B = \frac{e\hbar}{2m_e} = 9.274\ X\ 10^{-24}\ JT^{-1}, \tag{23}$$

The magnetic field of the electron shown in Figure 4 is given by

$$\mathbf{H} = \frac{e\hbar}{m_e r_n^3}(\mathbf{i}_r \cos\theta - \mathbf{i}_\theta \sin\theta) \qquad \text{for } r < r_n \tag{24}$$

$$\mathbf{H} = \frac{e\hbar}{2m_e r^3}(\mathbf{i}_r 2\cos\theta - \mathbf{i}_\theta \sin\theta) \qquad \text{for } r > r_n \tag{25}$$

The energy stored in the magnetic field of the electron is

$$E_{mag} = \frac{1}{2}\mu_o \int_0^{2\pi}\int_0^{\pi}\int_0^{\infty} H^2 r^2 \sin\theta dr d\theta d\Phi \tag{26}$$

$$E_{mag\ total} = \frac{\pi \mu_o e^2 \hbar^2}{m_e^2 r_1^3} \tag{27}$$

d. Stern-Gerlach Experiment

The Stern-Gerlach experiment implies a magnetic moment of one Bohr magneton and an associated angular momentum quantum number of 1/2. Historically, this quantum number is called the spin quantum number, s ($s = \frac{1}{2}; m_s = \pm\frac{1}{2}$). The superposition of the vector projection of the orbitsphere angular momentum on to an axis S that precesses about the z-axis called the spin axis at an angle of $\theta = \frac{\pi}{3}$ and an angle of $\phi = \pi$ with respect to $\langle \mathbf{L}_{xy} \rangle_{\Sigma \Delta\alpha}$ is

$$\mathbf{S} = \pm\sqrt{\frac{3}{4}}\hbar \tag{28}$$

S rotates about the z-axis at the Larmor frequency. $\langle \mathbf{S}_z \rangle$, the time averaged projection of the orbitsphere angular momentum onto the axis of the applied magnetic field is

$$\langle \mathbf{L}_z \rangle_{\Sigma \Delta\alpha} \pm \frac{\hbar}{2}. \tag{29}$$

e. Electron g Factor

Conservation of angular momentum of the orbitsphere permits a discrete change of its "kinetic angular momentum" ($\mathbf{r}\times m\mathbf{v}$) by the applied magnetic field of $\frac{\hbar}{2}$, and concomitantly the "potential angular momentum" ($\mathbf{r}\times e\mathbf{A}$) must change by $-\frac{\hbar}{2}$.

$$\Delta\mathbf{L}=\frac{\hbar}{2}-\mathbf{r}\times e\mathbf{A} \tag{30}$$

$$=\left[\frac{\hbar}{2}-\frac{e\phi}{2\pi}\right]\hat{z} \tag{31}$$

In order that the change of angular momentum, $\Delta\mathbf{L}$, equals zero, ϕ must be $\Phi_0=\frac{h}{2e}$, the magnetic flux quantum. The magnetic moment of the electron is parallel or antiparallel to the applied field only. During the spin-flip transition, power must be conserved. Power flow is governed by the Poynting power theorem,

$$\nabla\bullet(\mathbf{E}\times\mathbf{H})=-\frac{\partial}{\partial t}\left[\frac{1}{2}\mu_o\mathbf{H}\bullet\mathbf{H}\right]-\frac{\partial}{\partial t}\left[\frac{1}{2}\varepsilon_o\mathbf{E}\bullet\mathbf{E}\right]-\mathbf{J}\bullet\mathbf{E} \tag{32}$$

Eq. (33) gives the total energy of the flip transition which is the sum of the energy of reorientation of the magnetic moment (1st term), the magnetic energy (2nd term), the electric energy (3rd term), and the dissipated energy of a fluxon treading the orbitsphere (4th term), respectively,

$$\Delta E_{mag}^{spin}=2\left(1+\frac{\alpha}{2\pi}+\frac{2}{3}\alpha^2\left(\frac{\alpha}{2\pi}\right)-\frac{4}{3}\left(\frac{\alpha}{2\pi}\right)^2\right)\mu_B B \tag{33}$$

$$\Delta E_{mag}^{spin}=g\mu_B B \tag{34}$$

where the stored magnetic energy corresponding to the $\frac{\partial}{\partial t}\left[\frac{1}{2}\mu_o\mathbf{H}\bullet\mathbf{H}\right]$ term increases, the stored electric energy corresponding to the $\frac{\partial}{\partial t}\left[\frac{1}{2}\varepsilon_o\mathbf{E}\bullet\mathbf{E}\right]$ term increases, and the $\mathbf{J}\bullet\mathbf{E}$ term is dissipative. The spin-flip transition can be considered as involving a magnetic moment of g times that of a Bohr magneton. The g factor is redesignated the fluxon g factor as opposed to the anomalous g factor. The calculated value of $\frac{g}{2}$ is

1.001 159 652 137 [3]. The experimental value of $\frac{g}{2}$ is 1.001 159 652 188(4) [42].

f. Hydride Ion

A novel hydride ion having extraordinary chemical properties given by Mills [3] is predicted to form by the reaction of an electron with a hydrino (Eq. (35)). The resulting hydride ion is referred to as a hydrino hydride ion, designated as $H^-(1/p)$.

$$H\left[\frac{a_H}{p}\right]+e^- \rightarrow H^-(1/p) \tag{35}$$

The hydrino hydride ion is distinguished from an ordinary hydride ion having a binding energy of 0.8 eV for $p=1$. The hydrino hydride ion is predicted [3] to comprise a hydrogen nucleus and two indistinguishable electrons at a binding energy according to the following formula:

$$Binding\ Energy = \frac{\hbar^2\sqrt{s(s+1)}}{8\mu_e a_0^2\left[\frac{1+\sqrt{s(s+1)}}{p}\right]^2} - \frac{\pi\mu_0 e^2\hbar^2}{m_e^2 a_0^3}\left(1+\frac{2^2}{\left[\frac{1+\sqrt{s(s+1)}}{p}\right]^3}\right) \tag{36}$$

where p is an integer greater than one, $s=1/2$, π is pi, $\hbar$ is Planck's constant bar, μ_o is the permeability of vacuum, m_e is the mass of the electron, μ_e is the reduced electron mass, a_o is the Bohr radius, and e is the elementary charge. The ionic radius is

$$r_1 = \frac{a_0}{p}\left(1+\sqrt{s(s+1)}\right);\ s=\frac{1}{2} \tag{37}$$

From Eq. (37), the radius of the hydrino hydride ion $H^-(1/p);\ p=\text{integer}$ is $\frac{1}{p}$ that of ordinary hydride ion, $H^-(1/1)$. From Eq. (37) radius of $H^-(1/2)$ is

$$r_1 = 0.93301 a_0 \tag{38}$$

where $p=2$. From Eq. (36), the binding energy E_B of $H^-(1/2)$ is

$$E_B = 3.0468\ eV\ (4069.4\ \text{Å}) \tag{39}$$

The radius of $H^-(1/4)$ is

$$r_1 = 0.46651 a_0 \tag{40}$$

where $p=2$, and the binding energy E_B of $H^-(1/4)$ is

$$E_B = 11.232\ eV\ (1103.8\ \text{Å}) \tag{41}$$

g. Hydride Ion Hyperfine Lines

For ordinary hydride ion H^-, a continuum is observed at shorter wavelengths of the ionization or binding energy referred to as the bound-free continuum. For typical conditions in the photosphere, Figure 5 shows the continuous absorption coefficient $\kappa_C(\lambda)$ of the Sun [43]. In the visible and infrared, the hydride ion H^- is the dominant absorber. Its free-free continuum starts at $\lambda = 1.645\,\mu m$, corresponding to the ionization energy of $0.745\,eV$ for H^- with strongly increasing absorption towards the far infrared. The ordinary hydride spectrum recorded on the Sun is representative of the hydride spectrum in a very hot plasma.

Hydride ions formed by the reaction of hydrogen or hydrino atoms with free electrons with a kinetic energy distribution give rise to the bound-free emission band to shorter wavelengths than the ionization or binding energy due to the release of the electron kinetic energy and the hydride ion binding energy. As shown by Eq. (36), the energies for the formation of hydrino hydride ions are much greater, and with sufficient spectroscopic resolution, it may be possible to resolve hyperfine structure in the corresponding bound-free band due to interactions of the free and bound electrons. The derivation of the hyperfine lines follows.

Consider a free electron binding to a hydrino atom to form a hydrino hydride ion. The total angular momentum of an electron is $\hbar$. During binding of the free electron, the bound electron produces a magnetic field at the free electron given by Eq. (25). Thus, for radial distances greater than the radius of the hydride ion, the magnetic field is equivalent to that of a magnetic dipole of a Bohr magneton at the origin. The energy of interaction of a magnetic dipole with the magnetic field of the bound electron E_{ss}, the spin-spin energy, is given by Eq. (34)—the product of the electron g factor given by Eq. (33), the magnetic moment of the free electron, a Bohr magneton given by Eq. (23), and the magnetic flux which follows from Eq. (25).

$$E_{ss} = g\mu_B\mu_0 H = g\mu_B B = g\frac{\mu_0}{r^3}\left(\frac{e\hbar}{2m_e}\right)^2 \tag{42}$$

where μ_0 is the permeability of free space, r is the radius of hydride ion $H^-(n = 1/p)$ given by Eq. (37), and p is an integer. E_{ss} for $H^-(1/2)$ is given

by

$$E_{xx} = 0.011223\, eV \tag{43}$$

where the radius is given by Eq. (38). When a free electron binds to the hydrino atom $H(1/2)$ to form a hydride ion $H^-(1/2)$, a photon is emitted with a minimum energy equal to the binding energy ($E_B = 3.0468\, eV$). Any kinetic energy that the free electron possess must increase the energy of the emitted photon. The interaction of the two electrons quantizes this emission by the same mechanism as that observed in the Stern Gerlach experiment—quantization of flux linkage. Superconducting Quantum Interference Devices (SQUIDs) or wire loops linked to SQUIDs also show quantization of flux and the corresponding energies as shown in Chp 37 of Ref. 3.

In the Stern-Gerlach experiment, a magnetic field is applied along the z-axis called the spin axis. S, the projection of the angular momentum of an electron onto an axis which precesses about the z-axis, is $\pm\sqrt{\frac{3}{4}}\hbar$. S rotates about the z-axis at the Larmor frequency, and $\langle S_z \rangle$, the time averaged projection of the electron angular momentum onto the axis of the applied magnetic field is $\pm\frac{\hbar}{2}$ [3]. As given in Sec. I D e, the electron links flux in units of the magnetic flux quantum $\Phi_0 = \frac{h}{2e}$ during a Stern-Gerlach transition which conserves the angular momentum of the electron of $\hbar$. Due to the field of the bound electron, the free electron possessing kinetic energy will precess with a precessional angular momentum as well as an intrinsic angular momentum of $\pm\sqrt{s(s+1)}\hbar = \pm\sqrt{\frac{3}{4}}\hbar$. In order to conserve angular momentum of both electrons as the bound electron links an integer number of fluxons due to the free electron, the total angular momentum of the free electron must have a magnitude that is an integer number of $\frac{\hbar}{\sqrt{s(s+1)}}$. The corresponding fluxon energy E_Φ follows from Eq. (33) derived previously [3] wherein the angular momentum corresponding to the Bohr magneton, $\hbar$, is replaced by $j\frac{\hbar}{\sqrt{s(s+1)}}$, and the magnetic flux density B is given by the ratio of the flux to the area.

$$E_\Phi = j(g-2)\frac{\mu_B}{\sqrt{s(s+1)}}B = j(g-2)\frac{\mu_B}{\sqrt{s(s+1)}}\left(\frac{j\Phi_o}{A}\right) = j^2(g-2)\frac{\mu_B}{\sqrt{s(s+1)}}B$$
$$= j^2(g-2)\frac{\mu_B}{\sqrt{s(s+1)}}\frac{\mu_0}{r^3}\left(\frac{e\hbar}{2m_e}\right) \quad (44)$$

where j is an integer, $s=1/2$, and A is the area linked by the integer number of fluxons as given previously [3]. With the radius given by Eq. (38), the fluxon energy E_Φ of $H^-(1/2)$ is given by

$$E_\Phi = j^2(g-2)\frac{\mu_B}{\sqrt{s(s+1)}}\frac{\mu_0}{r^3}\left(\frac{e\hbar}{2m_e}\right) = j^2 3.0056\ X\ 10^{-5}\ eV \quad (45)$$

The energies of the hyperfine lines E_{HF}, are given by the sum of the binding energy (Eqs. (36) and (39)), the spin-spin energy (Eqs. (42) and (43)), and the fluxon energy (Eqs. (44) and (45)).

$$E_{HF} = E_\Phi + E_{ss} + E_B = j^2 3.0056\ X\ 10^{-5} + 0.011223 + 3.0468\ eV$$
(j is an integer) (46)
$$= j^2 3.0056\ X\ 10^{-5} + 3.0580\ eV$$

h. Spectroscopic Determination of the Bound-Free Hyperfine Levels of $H^-(1/2)$

Extreme ultraviolet (EUV) spectra recorded on microwave discharges of helium with 2% hydrogen were previously reported [8, 9, 19]. He^+ ionizes at $54.417\ eV$ which is $2 \cdot 27.2\ eV$, and novel emission lines were observed with energies of $q \cdot 13.6\ eV$ where $q = 1,2,3,4,6,7,8,9,11,12$ or these lines inelastically scattered by helium atoms wherein $21.2\ eV$ was absorbed in the excitation of $He(1s^2)$ to $He(1s^1 2p^1)$. These lines were identified as hydrogen transitions to electronic energy levels below the "ground" state corresponding to fractional quantum numbers. The hydrino catalysis product may further react with a source of electrons to form the corresponding hydride ion. Each of K^+/K^+, Rb^+, Cs, and Ar^+ are predicted to catalyze hydrogen to form $H\left[\frac{a_H}{2}\right]$ which reacts with an electron to form $H^-(1/2)$. A potassium atom is predicted to catalyze hydrogen to form $H\left[\frac{a_H}{4}\right]$ which reacts with an electron to form $H^-(1/4)$. Several studies including EUV and high resolution visible spectroscopy on rt-plasmas from several salt or metal catalysts confirmed the catalyst

mechanism and the predicted novel hydride ions. Exemplary studies include:

1.) the observation of continuum state emission of Cs^{2+} and Ar^{2+} at 533 Å and 456 Å, respectively, with the absence of the other corresponding Rydberg series of lines from these species which confirmed the resonant nonradiative energy transfer of $27.2\,eV$ from atomic hydrogen to the catalysts atomic Cs or Ar^{+} [15],

2.) the spectroscopic observation of the predicted hydride ion $H^{-}(1/2)$ of hydrogen catalysis by either Cs atom or Ar^{+} catalyst at 4070 Å corresponding to its predicted binding energy of $3.05\,eV$ [11, 15],

3.) the observation of characteristic emission from K^{3+} which confirmed the resonant nonradiative energy transfer of $3 \cdot 27.2\,eV$ from atomic hydrogen to atomic K [14],

4.) the spectroscopic observation of the predicted $H^{-}(1/4)$ ion of hydrogen catalysis by K catalyst at 1100 Å corresponding to its predicted binding energy of $11.2\,eV$ [14],

5.) the observation of characteristic emission from Rb^{2+} which confirmed the resonant nonradiative energy transfer of $27.2\,eV$ from atomic hydrogen to Rb^{+} [13],

6.) the spectroscopic observation of the predicted $H^{-}(1/2)$ ion of hydrogen catalysis by Rb^{+} catalyst at 4070 Å corresponding to its predicted binding energy of $3.05\,eV$ [11, 13],

7.) the high resolution visible spectroscopic observation from rt-plasmas and plasma electrolysis cells of the predicted $H^{-}(1/2)$ ion of hydrogen catalysis by each of K^{+}/K^{+}, Rb^{+}, Cs, and Ar^{+} at 4070 Å corresponding to its predicted binding energy of $3.05\,eV$ [11-12],

Evidence was also previously presented that emission from lower-energy hydrogen atoms and molecules, as well as hydride ions was

observed from the Sun and interstellar medium [3, 6, 8, 10].

According to Eq. (42) and (44), the predicted electron interactions for $H^-(1/2)$ are 8 times more energetic than those of ordinary hydride ion. Identification of the $H^-(1/2)$ hydride ion was sought using high resolution spectroscopy of rt-plasma cell emission from Rb^+ and K^+/K^+ catalysts which were each predicted to form $H(1/2)$ which further reacts to form $H^-(1/2)$. The spectrometer had a sufficiently high resolution (±0.06 Å) to determine whether the predicted hyperfine structure due to bound-free electron-electron interactions occurred during the formation of the hydride $H^-(1/2)$ in rt-plasma formed by K^+/K^+ and Rb^+ catalysts.

II. EXPERIMENTAL

A. EUV spectroscopy recorded on rt-plasmas

EUV spectra, 6562 Å Balmer α line width measurements, and high resolution visible spectra were recorded on light emitted from rt-plasmas of hydrogen with KNO_3 and $RbNO_3$. The experimental set up shown in Figure 6 comprised a quartz cell which was 500 mm in length and 50 mm in diameter. The entire quartz cell was enclosed in an Alumina insulation package. Several K-type thermocouples were located in the insulation. The thermocouples were monitored with a multichannel computer data acquisition system. A Pyrex cap sealed to the quartz cell with a Viton O ring and a C-clamp incorporated ports for gas inlet, outlet, and photon detection. A tungsten filament (0.508 mm in diameter and 800 cm in length, total resistance ~2.5 ohm) heater and hydrogen dissociator were in the quartz tube as well as a cylindrical titanium screen (300 mm long and 40 mm in diameter) that served as a second hydrogen dissociator. The filament was coiled on a grooved ceramic tube support to maintain its shape when heated. The return lead passed through the inside of the ceramic tube. The nitrate test materials were coated on a titanium screen dissociator by the method of wet impregnation. The screen was coated by dipping it in a 0.6 M KNO_3/10% H_2O_2 or 0.6 M $RbNO_3$/10% H_2O_2, and the crystalline material was dried on the surface by heating for 12 hours in a drying oven at 130 °C. A new dissociator was used for each experiment. The titanium screen was electrically floated with power applied to the

filament. In each test, power was applied to the filament by a DC power supply which was controlled by a constant power controller. The power applied to the filament was 300 W. The voltage across the filament was about 40 V and the current was about 6.25 A at 250 W. The temperature of the tungsten filament was estimated to be in the range 1100 to 1500 °C. The external cell wall temperature was about 700 °C.

The cell was operated under gas flow conditions while maintaining a constant gas pressure in the cell. The hydrogen gas was ultrahigh purity. The gas pressure inside the cell was maintained at about 300 mtorr with a hydrogen flow rate of 5.5 sccm controlled by a 0-20 sccm range mass flow controller (MKS 1179A21CS1BB) with a readout (MKS type 246). The cell pressure was monitored by a 0-10 torr MKS Baratron absolute pressure gauge.

The light emission was introduced to an EUV spectrometer for spectral measurement. The spectrometer was a McPherson 0.2 meter monochromator (Model 302, Seya-Namioka type) equipped with a 1200 lines/mm holographic grating with a platinum coating. The wavelength region covered by the monochromator was 50–5600 Å. A channel electron multiplier (CEM) was used to detect the EUV light. The wavelength resolution was about 2 Å (FWHM) with an entrance and exit slit width of 10 μm. The vacuum inside the monochromator was maintained below $5 X 10^{-4}$ Torr by a turbo pump. The Lyman α emission was recorded as a function of time after the filament was turned on. In each case, the EUV spectrum (900–1300 Å) of the rt-plasma cell emission was recorded at about the point of the maximum Lyman α emission to confirm the rt-plasma before the line broadening and high resolution visible spectrum in the region of 4070.0 Å were recorded. The EUV spectrum was also recorded on light emitted from a hydrogen glow discharge maintained according to methods reported previously [8] that served as a control for measurements recorded on light emitted from rt-plasmas of hydrogen with KNO_3.

B. Balmer α line broadening and high resolution visible spectroscopy recorded on rt-plasmas

The plasma emission from each rt-plasma maintained in the

filament heated cell was fiber-optically coupled through a 220F matching fiber adapter positioned 2 cm from the cell wall to a high resolution visible spectrometer with a resolution of ±0.06 Å over the spectral range 1900-8600 Å. The spectrometer was a Jobin Yvon Horiba 1250 M with 2400 groves/mm ion-etched holographic diffraction grating. The entrance and exit slits were set to 20 μm. The spectrometer was scanned between 6555-6570 Å using a 0.1 Å step size. The signal was recorded by a PMT with a stand alone high voltage power supply (950 V) and an acquisition controller. The data was obtained in a single accumulation with a 1 second integration time. In addition, the high resolution visible spectrum of each rt-plasma was recorded over the range 4000-4200 Å using the same methods as those of the line broadening measurements.

The width of the 6562 Å Balmer α line and the high resolution visible spectrum (4000-4200 Å) were also recorded on light emitted from a hydrogen glow discharge cell maintained according to methods reported previously [21]. The light introduced into the 220F matching fiber adapter positioned 2 cm from a sapphire window in the discharge cell wall served as a control for measurements recorded on light emitted from rt-plasmas of hydrogen with KNO_3 and $RbNO_3$.

III. RESULTS AND DISCUSSION

A. EUV Spectroscopy

The intensity of the Lyman α emission as a function of time from the gas cell at a cell temperature of 700 °C comprising a tungsten filament, a titanium dissociator, and 300 mtorr hydrogen with a flow rate of 5.5 sccm was tested for hydrogen alone and with potassium catalyst formed by hydrogen reduction and thermal decomposition of KNO_3. The cell was run with hydrogen but without any test material present to establish the baseline of the spectrometer. The intensity of the Lyman α emission as a function of time was measured for three hours, and no emission was observed. The intensity of the Lyman α emission as a function of time with vaporized potassium from KNO_3 was recorded. Strong EUV emission was observed from vaporized potassium catalyst only with hydrogen present.

The EUV spectrum (900 – 1300 Å) of the cell emission of a control hydrogen glow discharge is shown in Figure 7. The EUV spectrum (900 – 1300 Å) of the potassium rt-plasma cell emission recorded at about the point of the maximum Lyman α emission is shown in Figure 8. No emission was observed in the absence of hydrogen, and no emission occurred until the catalyst was vaporized as indicated by the appearance of KNO_3 crystals and a metal coating in the cap of the cell over the course of the experiment. Potassium is predicted to form the hydride $H^-(1/4)$ with emission in the region of 1100 Å (Eq. (41)). Molecular hydrogen has peaks in this region as shown in Figure 7. The broad peak in the region of 1100 Å was assigned to $H^-(1/4)$ based on comparison of the ratio of the intensity of this peak and nearby hydrogen molecular lines to the ratio at the same wavelengths from the control as described previously [14]. The novel 1100 Å continuum peak was observed only with potassium and atomic hydrogen present over an extended reaction time. As shown in Figures 7 & 8, the Lyman β and Lyman δ lines of the potassium gas cell at 1026 Å and 973 Å, respectively, have a much greater intensity relative to Lyman α line at 1216 Å than those of the hydrogen glow discharge. For example, the rt-plasma Lyman β to α ratio was very high—1.3 versus 0.13 for the control which indicates a high plasma temperature. These results are consistent with the formation of $H^-(1/4)$ from the catalysis of atomic hydrogen by $K(m)$.

The hydride ion $H^-(1/4)$ has been reported previously [29]. *KHI* containing $H^-(1/4)$ was synthesized by reaction of potassium metal, atomic hydrogen, and *KI*. The XPS spectrum of the product blue crystals differed from that of *KI* by having additional features at 9.1 eV and 11.1 eV. The XPS peaks centered at 9.0 eV and 11.1 eV that did not correspond to any other primary element peaks were assigned to the $H^-(n=1/4)\,E_b=11.2\,eV$ hydride ion (Eq. (41)) in two different chemical environments where E_b is the predicted vacuum binding energy. Furthermore, the reported minimum heats of formation of *KHI* by the catalytic reaction of potassium with atomic hydrogen and *KI* were over $-2000\,kJ/mole\,H_2$ compared to the enthalpy of combustion of hydrogen of $-241.8\,kJ/mole\,H_2$ [34].

B. Balmer α line broadening recorded on rt-plasmas

Line broadening of the hydrogen Balmer lines provides a sensitive measure of the number and energy of excited hydrogen atoms in a plasma. To further characterize the plasma parameters of rt-plasmas, the width of the 6562 Å Balmer α line was recorded on light emitted from rt-plasmas formed from hydrogen with a gaseous atom or ion which ionizes at integer multiples of the potential energy of atomic hydrogen. The results of the 6562 Å Balmer α line width measured with a high resolution (±0.06 Å) visible spectrometer on light emitted from rt-plasmas of hydrogen with KNO_3 and $RbNO_3$ are shown in Figures 9 and 10, respectively. To illustrate the method of displaying each line broadening result as an unsmoothed curve, the corresponding raw data points are also shown that further show the scatter in the data. The Balmer α line width and energetic hydrogen atom densities and energies given in Table 1 were calculated from the broadening using the method of Videnocic et al. [44]. Significant line broadening of 17 and 9 eV and an atom density of $4\,X\,10^{11}$ *and* $6\,X\,10^{11}$ $atoms/cm^3$ were observed from rt-plasmas of hydrogen formed with K^+/K^+ and Rb^+ catalysts, respectively. Whereas, a glow discharge of hydrogen maintained at the same total pressure with an electric field strength that was at least two order of magnitude greater than the 1 V/cm field of the filament cell showed no excessive broadening corresponding to an average hydrogen atom temperature of $\approx 3\,eV$.

In the characterization of the plasmas of Grimm-type discharges with a hollow anode, Videnocic et al. [44] and M. Kuraica and N. Konjevic [45] analyzed the broadening data in terms of Stark and Doppler effects wherein acceleration of charges such as H^+, H_2^+, and H_3^+ in the high fields (e. g. over $10\,kV/cm$) which were present in the cathode fall region was used to explain the Doppler component. In our experiments, the results could not be explained by Stark or thermal broadening or electric field acceleration of charged species since the measured field of the incandescent heater was extremely weak, 1 V/cm, corresponding to a broadening much less than $1\,eV$. Rather the source of the excessive line broadening is consistent with that of EUV emission, an energetic reaction caused by a resonance energy transfer between hydrogen atoms and

K^+/K^+ or Rb^+ catalyst.

Rt-plasmas formed with hydrogen-potassium mixtures have been reported previously [26-27] wherein the plasma decayed with a two second half-life when the electric field was set to zero. This was the thermal decay time of the filament which dissociated molecular hydrogen to atomic hydrogen. This experiment showed that hydrogen line emission was occurring even though the voltage between the heater wires was set to and measured to be zero and indicated that the emission was due to a reaction of potassium atoms with atomic hydrogen. Potassium atoms ionize at an integer multiple of the potential energy of atomic hydrogen, $m \cdot 27.2\,eV$. The enthalpy of ionization of K to K^{3+} has a net enthalpy of reaction of $81.7426\,eV$, which is equivalent to $m=3$.

An excessive afterglow duration was observed for rt-plasmas of hydrogen and certain alkali ions that were recorded via EUV spectroscopy and the hydrogen Balmer and alkali line emissions in the visible range [27]. The observed plasma formed at low temperatures (e.g. $\approx 10^3\,K$) from atomic hydrogen generated at a tungsten filament that heated a titanium dissociator and one of potassium, rubidium, cesium, and their carbonates and nitrates. These atoms and ions ionize to provide a net enthalpy of reaction of an integer multiple of the potential energy of atomic hydrogen ($m \cdot 27.2\,eV$, $m=$integer) to within 0.17 eV and comprise only a single ionization in the case of a potassium or rubidium ion. Whereas, the chemically similar atoms of sodium and sodium and lithium carbonates and nitrates which do not ionize with these constraints caused no emission. To test the electric dependence of the emission, the weak electric field of about 1 V/cm was set and measured to be zero in $< 0.5\,X\,10^{-6}$ sec. An afterglow duration of about one to two seconds was recorded in the case of potassium, rubidium, cesium, K_2CO_3, $RbNO_3$, and $CsNO_3$. Hydrogen line or alkali line emission was occurring even though the voltage between the heater wires was set to and measured to be zero. These atoms and ions ionize to provide a net enthalpy of reaction of an integer multiple of the potential energy of atomic hydrogen to within less than the thermal energies at $\approx 10^3\,K$ and comprise only a single ionization in the case of a potassium or rubidium ion. Since the thermal decay time of the filament for dissociation of molecular hydrogen to atomic hydrogen was similar to the rt-plasma

afterglow duration, the emission was determined to be due to a reaction of atomic hydrogen with each of the atoms or ions that did not require the presence of an electric field to be functional.

C. High resolution visible spectroscopy recorded on rt-plasmas

The high resolution visible spectra (4000-4060 Å) and (4060-4090 Å) recorded on the emission of a control hydrogen glow discharge plasma are shown in Figures 11 and 12, respectively. Only weak hydrogen molecular peaks were observed.

The high resolution visible spectrum in the region of 4000 Å to 4090 Å recorded on the emission of a rt-plasma formed with K^+/K^+ catalyst from vaporized KNO_3 is shown in Figure 13 with the expanded views of the 4000-4060 Å and 4060-4090 Å regions shown in Figures 14 and 15, respectively. A broad peak consistent with a hydride ion was observed at 4070.0 Å with a FWHM of 1.4 Å. This peak overlaps the predicted threshold for binding energy of $H^-(1/2)$ given by Eq. (39). The 4070.0 Å peak was not observed in the hydrogen glow discharge plasma as shown in Figures 11 and 12. O II lines at 4069.623, 4069.881, and 4071.238 Å were eliminated due to the absence of O I lines at 3947.29, 3947.48, 3947.58, 3954.60, and 4054.77 Å. C III lines at 4070.26 and 4068.916 Å were eliminated due to the absence of C I lines which were outside of the region of 4070 Å or C II lines at 3918.96 and 3920.68 Å. Furthermore, the presence of the O II or C III lines would be extraordinary since the ionization energy required for O II is above the first ionization energy of $13.62\,eV$, and the energies required for C III are above the sum of the first and second ionization energies of $11.26\,eV$ and $24.38\,eV$, respectively [39]. The novel 4070.0 Å peak which could not be assigned to a known peak was assigned to $H^-(1/2)$. Other peaks in the rt-plasma that partially covered some of the hyperfine peaks were assigned to molecular hydrogen and K I. In addition, K II was observed outside this region at 4829 Å which confirmed the presence of the catalyst K^+/K^+.

Since the $H^-(1/2)$ peak is broad, it consequently contributes to the broadening of the hyperfine lines. Thus, a better determination of the hyperfine energies under experimental conditions is to use the maximum

of the hydride peak as the parameter E_B in Eq. (46). Substitution of the energy, 3.0463 eV, corresponding to the wavelength of the maximum of the observed hydride peak, 4070.0 Å, into Eq. (46) for E_B gives

$$E_{HF} = E_{\Phi} + E_{\pi} + E_B = j^2 3.0056\ X\ 10^{-5} + 0.011223 + 3.0463\ eV \quad (j \text{ is an integer}) \quad (47)$$

$$= j^2 3.0056\ X\ 10^{-5} + 3.0575\ eV$$

The predicted inverse Rydberg-type series that converges at increasing wavelengths and terminates at 3.0575 eV was observed as shown in Figures 13 and 14.

The inverse Rydberg-type series of broad emission lines was not observed in the hydrogen glow discharge plasma as shown in Figures 11 and 12. Other possibilities such as rotational transitions of diatomic molecules were also eliminated. Emission in the 4000-4060 Å region could only correspond to an electronic transition with emission from vibrational as well as rotational levels. No vibrational or other related electronic bands were observed. Diatomic molecules other than H_2 have equally spaced rotational levels which may have $\approx 10^{-3}$ energies, but the observed lines matched a second order integer relationship as opposed to a linear one. Furthermore, the system was run under hydrogen flow conditions with continuous pumping which made improbable the presence of a detectable concentration of gaseous molecules other than hydrogen. And, the possible diatomic molecules, NO, N_2, O_2, and OH, were further eliminated as the source of the Rydberg-type series based on their known spectra such as those shown in Figure 3 of Refs. 46-47. No emission was observed from these molecules as well as from oxygen or nitrogen atoms over the 900-1300 Å and 4000-4200 Å regions.

The high resolution visible spectrum in the region of 4000 Å to 4090 Å recorded on the emission of a rt-plasma formed with Rb^+ catalyst from vaporized $RbNO_3$ is shown in Figure 16 with the expanded views of the 4000-4060 Å and 4060-4090 Å regions are shown in Figures 17 and 18, respectively. The $H^-(1/2)$ hydride ion with a predicted binding energy of 3.0468 eV was observed as a broad peak at 4070.0 Å with a FWHM of 1.4 Å as shown in Figures 16 and 18. An inverse Rydberg-type series of broad emission lines shown in Figures 16 and 17 that converged at increasing wavelengths and terminated at about 3.0575 eV—the hydride spin-pairing energy plus the binding energy—matched the theoretical

hyperfine energies E_{HF} given by $E_{HF} = j^2 3.0056\,X\,10^{-5} + 3.0575\,eV$ for $j = 1$ to $j = 37$. The results are presented in Table 2. Other peaks in the rt-plasma that partially covered some of the hyperfine peaks were assigned to molecular hydrogen. In addition to hydrogen molecular lines, a Rb II peak was observed in Figure 18 which confirmed the presence of the catalyst Rb^+.

The emission spectra of the $H^-(1/2)$ hydride ion and the corresponding hyperfine lines were very reproducible. Three matching EUV spectra (4000-4060Å) of Rb^+ rt-plasmas that were equivalent to the spectrum of the K^+/K^+ and the Rb^+ rt-plasmas shown in Figures 14 and 17, respectively, are shown in Figure 19. The theoretical hyperfine energies, the observed energies, and the difference between the two are given in Table 2. The remarkable agreement is further evident in Figure 20 which shows the energies of the observed peaks overlaid on the plot of the theoretical energies given by Eq. (47).

IV. CONCLUSION

Each of an electron transfer between two K^+ ions and the ionization of a potassium atom or Rb^+ provide a reaction with a net enthalpy of an integer multiple of the potential energy of atomic hydrogen. The presence of each of the corresponding reactants formed the low applied temperature, extremely low voltage plasma called a resonance transfer or rt-plasma. For further characterization, the width of the 6562 Å Balmer α line was recorded on light emitted from rt-plasmas. Significant line broadening of 17 and 9 eV and an atom density of $4\,X\,10^{11}$ *and* $6\,X\,10^{11}$ *atoms/cm*^{3} were observed from a rt-plasma of hydrogen formed with potassium or K^+/K^+ and Rb^+ catalysts, respectively. These results could not be explained by Stark or thermal broadening or electric field acceleration of charged species since the measured field of the incandescent heater was extremely weak, 1 V/cm, corresponding to a broadening much less than $1\,eV$. Rather, the source of the excessive line broadening is consistent with that of EUV emission, an energetic reaction caused by a resonance energy transfer between hydrogen atoms and the catalyst.

The predicted $H^-(1/4)$ hydride ion of hydrogen catalysis by

potassium catalyst given by Eqs. (7-9) and Eq. (36) was observed spectroscopically at 1100 Å corresponding to its predicted binding energy of 11.2 eV.

The K^+/K^+ and Rb^+catalysis product, $H(1/2)$, given by Eqs. (4-6), and (10-12) respectively, was predicted to form hydride ion $H^-(1/2)$ given by Eq. (36). This hydride ion with a predicted binding energy of 3.0465 eV was observed by high resolution visible spectroscopy as a broad peak at 4070.0 Å with a FWHM of 1.4 Å. From the electron g factor, bound-free hyperfine structure lines of $H^-(1/2)$ were predicted with energies E_{HF} given by $E_{HF} = j^2 3.0022\,X\,10^{-5} + 3.0582\,eV$ (j is an integer) as an inverse Rydberg-type series that converges at increasing wavelengths and terminates at 3.0582 eV—the hydride spin-pairing energy plus the binding energy. Remarkable agreement between theory and experiment was observed for the lines corresponding to $j=1$ to $j=37$. Since the hyperfine lines of ordinary hydride ion are not sufficiently energetic to be resolved; whereas, those of $H^-(1/2)$ are, this is the first report of the observation of hyperfine energy levels of a hydride ion.

The release of energy from hydrogen as evidenced by the EUV emission must result in a lower-energy state of hydrogen. The present study identified the formation of novel hydride ions, $H^-(1/2)$ and $H^-(1/4)$. The formation of novel compounds based on novel hydride ions would be substantial evidence supporting catalysis of hydrogen as the mechanism of the observed EUV emission and further support the present spectroscopic identification of $H^-(1/2)$ and $H^-(1/4)$. Compounds containing novel hydride ions have been isolated as products of the reaction of atomic hydrogen with atoms and ions identified as catalysts in the present study and previously reported EUV studies [28-34]. The novel hydride compounds were identified analytically by techniques such as time of flight secondary ion mass spectroscopy, X-ray photoelectron spectroscopy, and ^1H nuclear magnetic resonance spectroscopy. For example, the time of flight secondary ion mass spectroscopy showed a large hydride peak in the negative spectrum. The X-ray photoelectron spectrum showed large metal core level shifts due to binding with the hydride as well as novel hydride peaks. The ^1H nuclear magnetic resonance spectrum showed significantly upfield shifted peaks which corresponded to and identified novel hydride ions as shown in Figure 21

reported previously [28].

The identification of novel hydride ions is indicative of a new field of hydrogen chemistry. Novel hydride ions may combine with other cations such as other alkali cations and alkaline earth, rare earth, and transition element cations. Numerous novel compounds may be synthesized with unique properties such as high stability relative to the corresponding compounds having ordinary hydride ions wherein the enthalpy of formation is very exothermic—at least $43.9\,eV/Hatom$ and $215.2\,eV/Hatom$ for $H^-(1/2)$ and $H^-(1/4)$, respectively, compared to the enthalpy of combustion of $1.48\,eV/Hatom$.

Since the net enthalpy released may be at least one hundred times that of combustion, the catalysis of atomic hydrogen represents a new source of energy with H_2O as the source of hydrogen fuel. Moreover, rather than air pollutants or radioactive waste, novel hydride compounds with potential broad commercial applications are the products [28-34]. Since the power is in the form of a plasma, direct high-efficiency, low cost energy conversion may be possible, thus, avoiding a heat engine such as a turbine [35-37] or a reformer-fuel cell system. Significantly lower capital costs and lower commercial operating costs than that of any known competing energy source are anticipated.

ACKNOWLEDGMENT

Special thanks to Alex Echezuria for preparing filament cells for plasma experiments and Bala Dhandapani for assisting with logistics and reviewing this manuscript.

REFERENCES

1. N. V. Sidgwick, *The Chemical Elements and Their Compounds*, Volume I, Oxford, Clarendon Press, (1950), p.17.
2. M. D. Lamb, *Luminescence Spectroscopy*, Academic Press, London, (1978), p. 68.
3. R. Mills, *The Grand Unified Theory of Classical Quantum Mechanics*, January 2000 Edition, BlackLight Power, Inc., Cranbury, New Jersey, Distributed by Amazon.com; September 2001 Edition posted at

www.blacklightpower.com.

4. R. Mills, "The Grand Unified Theory of Classical Quantum Mechanics", Global Foundation, Inc. Orbis Scientiae entitled *The Role of Attractive and Repulsive Gravitational Forces in Cosmic Acceleration of Particles The Origin of the Cosmic Gamma Ray Bursts*, (29th Conference on High Energy Physics and Cosmology Since 1964) Dr. Behram N. Kursunoglu, Chairman, December 14-17, 2000, Lago Mar Resort, Fort Lauderdale, FL, Kluwer Academic/Plenum Publishers, New York, pp. 243-258.
5. R. Mills, "The Grand Unified Theory of Classical Quantum Mechanics", Int. J. of Hydrogen Energy, in press.
6. R. Mills, "The Hydrogen Atom Revisited", Int. J. of Hydrogen Energy, Vol. 25, Issue 12, December, (2000), pp. 1171-1183.
7. R. Mills, The Nature of Free Electrons in Superfluid Helium—a Test of Quantum Mechanics and a Basis to Review its Foundations and Make a Comparison to Classical Theory, Int. J. Hydrogen Energy, Vol. 26, No. 10, (2001), pp. 1059-1096.
8. R. Mills, P. Ray, "Spectral Emission of Fractional Quantum Energy Levels of Atomic Hydrogen from a Helium-Hydrogen Plasma and the Implications for Dark Matter", Int. J. Hydrogen Energy, in press.
9. R. L. Mills, P. Ray, B. Dhandapani, J. He, "Spectroscopic Identification of Fractional Rydberg States of Atomic Hydrogen" J. Phys. Chem. Letts., submitted.
10. R. Mills, P. Ray, "Vibrational Spectral Emission of Fractional-Principal-Quantum-Energy-Level Hydrogen Molecular Ion", Int. J. Hydrogen Energy, in press.
11. R. Mills, P. Ray, M. Nansteel, W. Good, P. Jansson, B. Dhandapani, J. He, "Excessive Balmer α Line Broadening, Power Balance, and Novel Hydride Ion Product of Plasma Formed from Incandescently Heated Hydrogen Gas with Certain Catalysts", Int. J. Hydrogen Energy, submitted.
12. R. Mills, E. Dayalan, P. Ray, B. Dhandapani, J. He, "Highly Stable Novel Inorganic Hydrides from Aqueous Electrolysis and Plasma Electrolysis, submitted.
13. R. L. Mills, P. Ray, "Spectroscopic Identification of a Novel Catalytic Reaction of Rubidium Ion with Atomic Hydrogen and the Hydride Ion Product", Int. J. Hydrogen Energy, submitted.

14. R. Mills, P. Ray, Spectroscopic Identification of a Novel Catalytic Reaction of Potassium and Atomic Hydrogen and the Hydride Ion Product, Int. J. Hydrogen Energy, in press.
15. R. Mills, "Spectroscopic Identification of a Novel Catalytic Reaction of Atomic Hydrogen and the Hydride Ion Product", Int. J. Hydrogen Energy, Vol. 26, No. 10, (2001), pp. 1041-1058.
16. R. Mills and M. Nansteel, "Argon-Hydrogen-Strontium Plasma Light Source", IEEE Transactions on Plasma Science, submitted.
17. R. Mills, M. Nansteel, and Y. Lu, "Excessively Bright Hydrogen-Strontium Plasma Light Source Due to Energy Resonance of Strontium with Hydrogen", European Journal of Physics D, submitted.
18. R. Mills, J. Dong, W. Good, P. Ray, J. He, B. Dhandapani, Measurement of Energy Balances of Noble Gas-Hydrogen Discharge Plasmas Using Calvet Calorimetry, Int. J. Hydrogen Energy, submitted.
19. Randell L. Mills, P. Ray, B. Dhandapani, M. Nansteel, X. Chen, J. He, "New Power Source from Fractional Quantum Energy Levels of Atomic Hydrogen that Surpasses Internal Combustion", Spectrochimica Acta, submitted.
20. R. L. Mills, P. Ray, B. Dhandapani, J. He, "Comparison of Excessive Balmer α Line Broadening of Glow Discharge and Microwave Hydrogen Plasmas with Certain Catalysts" J. Phys. Chem., submitted.
21. R. L. Mills, A. Voigt, P. Ray, M. Nansteel, B. Dhandapani, "Measurement of Hydrogen Balmer Line Broadening and Thermal Power Balances of Noble Gas-Hydrogen Discharge Plasmas", Int. J. Hydrogen Energy, in press.
22. R. Mills, N. Greenig, S. Hicks, "Optically Measured Power Balances of Anomalous Discharges of Mixtures of Argon, Hydrogen, and Potassium, Rubidium, Cesium, or Strontium Vapor", Int. J. Hydrogen Energy, in press.
23. R. Mills, M. Nansteel, and Y. Lu, "Observation of Extreme Ultraviolet Hydrogen Emission from Incandescently Heated Hydrogen Gas with Strontium that Produced an Anomalous Optically Measured Power Balance", Int. J. Hydrogen Energy, Vol. 26, No. 4, (2001), pp. 309-326.
24. R. Mills, J. Dong, Y. Lu, "Observation of Extreme Ultraviolet Hydrogen Emission from Incandescently Heated Hydrogen Gas with Certain Catalysts", Int. J. Hydrogen Energy, Vol. 25, (2000), pp. 919-943.

25. R. Mills, "Observation of Extreme Ultraviolet Emission from Hydrogen-KI Plasmas Produced by a Hollow Cathode Discharge", Int. J. Hydrogen Energy, Vol. 26, No. 6, (2001), pp. 579-592.
26. R. Mills, "Temporal Behavior of Light-Emission in the Visible Spectral Range from a Ti-K2CO3-H-Cell", Int. J. Hydrogen Energy, Vol. 26, No. 4, (2001), pp. 327-332.
27. R. Mills, T. Onuma, and Y. Lu, "Formation of a Hydrogen Plasma from an Incandescently Heated Hydrogen-Catalyst Gas Mixture with an Anomalous Afterglow Duration", Int. J. Hydrogen Energy, Vol. 26, No. 7, July, (2001), pp. 749-762.
28. R. Mills, B. Dhandapani, M. Nansteel, J. He, A. Voigt, "Identification of Compounds Containing Novel Hydride Ions by Nuclear Magnetic Resonance Spectroscopy", Int. J. Hydrogen Energy, Vol. 26, No. 9, Sept. (2001), pp. 965-979.
29. R. Mills, B. Dhandapani, N. Greenig, J. He, "Synthesis and Characterization of Potassium Iodo Hydride", Int. J. of Hydrogen Energy, Vol. 25, Issue 12, December, (2000), pp. 1185-1203.
30. R. Mills, "Novel Inorganic Hydride", Int. J. of Hydrogen Energy, Vol. 25, (2000), pp. 669-683.
31. R. Mills, "Novel Hydrogen Compounds from a Potassium Carbonate Electrolytic Cell", Fusion Technology, Vol. 37, No. 2, March, (2000), pp. 157-182.
32. R. Mills, B. Dhandapani, M. Nansteel, J. He, T. Shannon, A. Echezuria, "Synthesis and Characterization of Novel Hydride Compounds", Int. J. of Hydrogen Energy, Vol. 26, No. 4, (2001), pp. 339-367.
33. R. Mills, "Highly Stable Novel Inorganic Hydrides", Journal of New Materials for Electrochemical Systems, in press.
34. R. Mills, W. Good, A. Voigt, Jinquan Dong, "Minimum Heat of Formation of Potassium Iodo Hydride", Int. J. Hydrogen Energy, Vol. 26, No. 11, Oct., (2001), pp. 1199-1208.
35. R. Mills, "BlackLight Power Technology-A New Clean Hydrogen Energy Source with the Potential for Direct Conversion to Electricity", Proceedings of the National Hydrogen Association, 12 th Annual U.S. Hydrogen Meeting and Exposition, *Hydrogen: The Common Thread*, The Washington Hilton and Towers, Washington DC, (March 6-8, 2001), pp. 671-697.

36. R. Mills, "BlackLight Power Technology-A New Clean Energy Source with the Potential for Direct Conversion to Electricity", Global Foundation International Conference on "Global Warming and Energy Policy", Dr. Behram N. Kursunoglu, Chairman, Fort Lauderdale, FL, November 26-28, 2000, Kluwer Academic/Plenum Publishers, New York, pp. 1059-1096.
37. R. Mayo, R. Mills, M. Nansteel, "On the Potential of Direct and MHD Conversion of Power from a Novel Plasma Source to Electricity for Microdistributed Power Applications", IEEE Transactions on Plasma Science, submitted.
38. C. J. Hardy, B. O. Field, J. Chem. Soc., (1963), pp. 5130-5134.
39. David R. Linde, *CRC Handbook of Chemistry and Physics*, 79 th Edition, CRC Press, Boca Raton, Florida, (1998-9), p. 10-175 to p. 10-177.
40. H. A. Haus, On the radiation from point charges, *American Journal of Physics*, **54**, 1126–1129 (1986).
41. D. A. McQuarrie, *Quantum Chemistry*, University Science Books, Mill Valley, CA, (1983), pp. 238-241.
42. R. S. Van Dyck, Jr., P. Schwinberg, H. Dehmelt, "New high precision comparison of electron and positron g factors", Phys. Rev. Lett., Vol. 21, (1987), p. 26-29.
43. M. Stix, *The Sun*, Springer-Verlag, Berlin, (1991), p. 136.
44. I. R. Videnocic, N. Konjevic, M. M. Kuraica, "Spectroscopic investigations of a cathode fall region of the Grimm-type glow discharge", Spectrochimica Acta, Part B, Vol. 51, (1996), pp. 1707-1731.
45. M. Kuraica, N. Konjevic, "Line shapes of atomic hydrogen in a plane-cathode abnormal glow discharge", Physical Review A, Volume 46, No. 7, October (1992), pp. 4429-4432.
46. C. O. Laux, R. J. Gessman, C. H. Kruger, "Measurements and modeling of the absolute spectral emission of air plasmas between 185 and 800 nm", Journal of Quantitative Spectroscopy and Radiative Transfer", (2001), submitted.
47. C. O. Laux, C. H. Kruger, R. N. Zare, "Diagnostics of atmospheric pressure air plasmas", www-krg.stanford.edu/kruger.html.

Table 1. Energetic hydrogen atom densities and energies for rt-plasmas determined from the 6562 Å Balmer α line width.

Plasma Gas	Hydrogen Atom Density[a] (10^{11} *atoms*/cm^3)	Hydrogen Atom Energy[b] (eV)
H_2	2	2-3[c]
K *and* $K^+/K^+/H_2$	4	15-18
Rb^+/H_2	6	8-10

[a] Approximate Calculated [44].
[b] Calculated [44].
[c] Measured on glow discharge according to method of Ref. 21.

Table 2. Calculated hyperfine emission lines of bound-free plasma emission of $H^-(1/2)$ and the observed lines.

Hyperfine Quantum Number j	Calculated Emission (eV) Eq. (47)	Calculated Emission (Å) Eq. (47)	Observed Lines (eV)	Observed Lines (Å)	Difference between Experimental and Calculated (eV)
1	3.0575	4055.1	3.0571	4055.6	-0.00041
2	3.0576	4055.0	3.0572	4055.5	-0.00039
3	3.0578	4054.8	3.0573	4055.4	-0.00045
4	3.0580	4054.5	3.0575	4055.2	-0.00052
5	3.0583	4054.1	3.0578	4054.7	-0.00044
6	3.0586	4053.7	3.0581	4054.4	-0.00051
7	3.0590	4053.2	3.0584	4054.0	-0.00062
8	3.0594	4052.6	3.0587	4053.5	-0.00072
9	3.0599	4051.9	3.0591	4053.0	-0.00084
10	3.0605	4051.1	3.0597	4052.2	-0.00080
11	3.0611	4050.3	3.0605	4051.2	-0.00068
12	3.0618	4049.4	3.0613	4050.1	-0.00055
13	3.0626	4048.4	3.0622	4048.9	-0.00038
14	3.0634	4047.3	3.0630	4047.9	-0.00044
15	3.0643	4046.2	3.0639	4046.6	-0.00033
16	3.0652	4044.9	3.0651	4045.1	-0.00012
17	3.0662	4043.6	3.0663	4043.5	0.00010
18	3.0672	4042.2	3.0673	4042.1	0.00011
19	3.0684	4040.8	3.0684	4040.7	0.00006
20	3.0695	4039.2	3.0699	4038.8	0.00033
21	3.0708	4037.6	3.0705	4037.9	-0.00022
22	3.0720	4035.9	3.0716	4036.5	-0.00045
23	3.0734	4034.1	3.0730	4034.6	-0.00038
24	3.0748	4032.3	3.0744	4032.8	-0.00039
25	3.0763	4030.4	3.0758	4031.0	-0.00053
26	3.0778	4028.3	3.0774	4028.9	-0.00042
27	3.0794	4026.3	3.0790	4026.8	-0.00043
28	3.0811	4024.1	3.0807	4024.6	-0.00038
29	3.0828	4021.9	3.0825	4022.3	-0.00032
30	3.0846	4019.6	3.0843	4019.9	-0.00026
31	3.0864	4017.2	3.0862	4017.5	-0.00023
32	3.0883	4014.7	3.0881	4014.9	-0.00013
33	3.0902	4012.2	3.0902	4012.2	-0.00004
34	3.0922	4009.6	3.0922	4009.6	-0.00001
35	3.0943	4006.9	3.0943	4006.9	-0.00003
36	3.0965	4004.1	3.0964	4004.2	-0.00005
37	3.0986	4001.3	3.0986	4001.4	-0.00007

Figure Captions

Figure 1. The orbitsphere is a two dimensional spherical shell with the Bohr radius of the hydrogen atom.

Figure 2. The current pattern of the orbitsphere from the perspective of looking along the z-axis. The current and charge density are confined to two dimensions at $r_n = nr_1$. The corresponding charge density function is uniform.

Figure 3. The orbital function modulates the constant (spin) function (shown for t = 0; cross-sectional view).

Figure 4. The magnetic field of an electron orbitsphere.

Figure 5. Continuum absorption coefficient (per particle) in the solar atmosphere showing a discontinuity at $1.645\,\mu m$, the wavelength corresponding to the ordinary hydride ion H^- ionization energy, and the bound-free continuum of H^- at shorter wavelengths.

Figure 6. The experimental set up comprising a filament gas cell light source and an EUV spectrometer which was differentially pumped.

Figure 7. The EUV spectrum (900 – 1300 Å) of the cell emission of a control hydrogen glow discharge.

Figure 8. The EUV spectrum (900 – 1300 Å) of the potassium rt-plasma cell emission. The increase in intensity at 1100 Å compared to hydrogen emission alone was assigned to a contribution from $H^-(1/4)$. The Lyman β to α ratio was also very high—1.3 versus 0.13 for the control.

Figure 9. The 6562 Å Balmer α line width recorded with a high resolution (±0.06 Å) visible spectrometer on a rt-plasma formed with K^+/K^+ catalyst. Significant broadening was observed corresponding to an average hydrogen atom temperature of $17\,eV$.

Figure 10. The 6562 Å Balmer α line width recorded with a high resolution (±0.06 Å) visible spectrometer on a rt-plasma formed with Rb^+ catalyst from $RbNO_3$. Significant broadening was observed corresponding to an average hydrogen atom temperature of $9\,eV$.

Figure 11. The high resolution visible spectrum in the region of 4000 Å to 4060 Å recorded on the emission of a control hydrogen glow discharge plasma. Only weak hydrogen molecular peaks were observed.

Figure 12. The high resolution visible spectrum in the region of

4060 Å to 4090 Å recorded on the emission of a control hydrogen glow discharge plasma. Only weak hydrogen molecular peaks were observed.

Figure 13. The high resolution visible spectrum in the region of 4000 Å to 4090 Å recorded on the emission of a rt-plasma formed with K^+/K^+ catalyst from vaporized KNO_3. The $H^-(1/2)$ hydride ion with a predicted binding energy of $3.0468\,eV$ was observed as a broad peak at 4070.0 Å with a FWHM of 1.4 Å. An observed inverse Rydberg-type series of broad emission lines that converged at increasing wavelengths and terminated at about $3.0575\,eV$—the hydride spin-pairing energy plus the binding energy—matched the theoretical hyperfine energies E_{HF} given by $E_{HF} = j^2 3.0056\,X\,10^{-5} + 3.0575\,eV$ for $j=1$ to $j=37$ as given in Table 2. Other peaks in the rt-plasma that partially covered some of the hyperfine peaks were assigned to K I and molecular hydrogen.

Figure 14. The 4000 Å to 4060 Å region of the Figure 13 spectrum to show an expanded view of the $H^-(1/2)$ emission hyperfine lines. Other peaks in the rt-plasma that partially covered some of the hyperfine peaks were assigned to K I and molecular hydrogen.

Figure 15. The 4060 Å to 4090 Å region of the Figure 13 spectrum to show an expanded view of the $H^-(1/2)$ binding energy emission. Other peaks in the rt-plasma were assigned to molecular hydrogen.

Figure 16. The high resolution visible spectrum in the region of 4000 Å to 4090 Å recorded on the emission of a rt-plasma formed with Rb^+ catalyst from vaporized $RbNO_3$. The $H^-(1/2)$ hydride ion with a predicted binding energy of $3.0468\,eV$ was observed as a broad peak at 4070.0 Å with a FWHM of 1.4 Å. An observed inverse Rydberg-type series of broad emission lines that converged at increasing wavelengths and terminated at about $3.0575\,eV$—the hydride spin-pairing energy plus the binding energy—matched the theoretical hyperfine energies E_{HF} given by $E_{HF} = j^2 3.0056\,X\,10^{-5} + 3.0575\,eV$ for $j=1$ to $j=37$ as given in Table 2. Other peaks in the rt-plasma were assigned to molecular hydrogen.

Figure 17. The 4000 Å to 4060 Å region of the Figure 16 spectrum to show an expanded view of the $H^-(1/2)$ emission hyperfine lines. Other peaks in the rt-plasma were assigned to molecular hydrogen.

Figure 18. The 4060 Å to 4090 Å region of the Figure 16 spectrum to show an expanded view of the $H^-(1/2)$ binding energy emission. Other peaks in the rt-plasma were assigned to Rb II and molecular hydrogen.

Figure 19. The three matching EUV spectra (4000-4060 Å) of Rb^+ rt-plasmas that were equivalent to the spectrum shown in Figure 17.

Figure 20. The plot of the theoretical hyperfine energies E_{HF} given by $E_{HF} = j^2 3.0056\, X\, 10^{-5} + 3.0575\, eV$ (Eq. (47)) for $j = 1$ to $j = 37$ and the energies observed for the inverse Rydberg-type series of broad emission lines shown in Figure 17 as given in Table 2. The agreement was remarkable.

Figure 21. (A) The ^1H MAS NMR spectrum of $KH*Cl$ relative to external tetramethylsilane (TMS). The resonance at 1.3 ppm was assigned to ordinary hydride ion. The large distinct upfield resonance at -4.4 identifies a hydride ion ($H*$) with a substantially smaller radius as compared with ordinary hydride since a smaller radius increases the shielding or diamagnetism, and it was assigned to a novel hydride ion of $KH*Cl$. (B) The ^1H MAS NMR spectrum of the control comprising an equal molar mixture of KH and KCl relative to external tetramethylsilane (TMS). Ordinary hydride ion has a resonance at 1.1 ppm and 0.8 ppm in the KH/KCl mixture and in KH. The presence of KCl does not shift the resonance of ordinary hydride as shown in Figure 21C. (C) The ^1H MAS NMR spectrum of the control KH relative to external tetramethylsilane (TMS).

Fig. 1

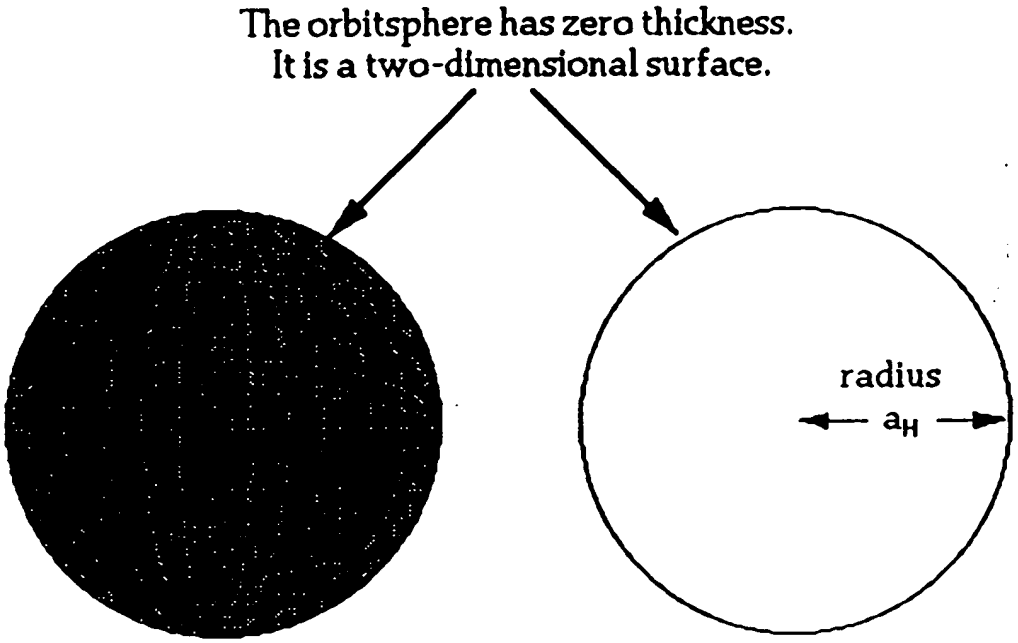
The orbitsphere has zero thickness.
It is a two-dimensional surface.
radius
a_H

Fig. 2

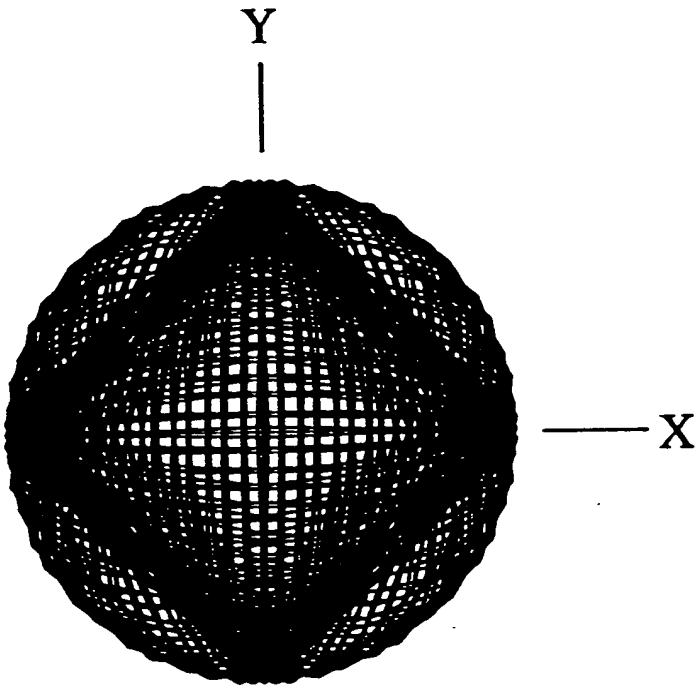

VIEW ALONG THE Z AXIS

Fig. 3

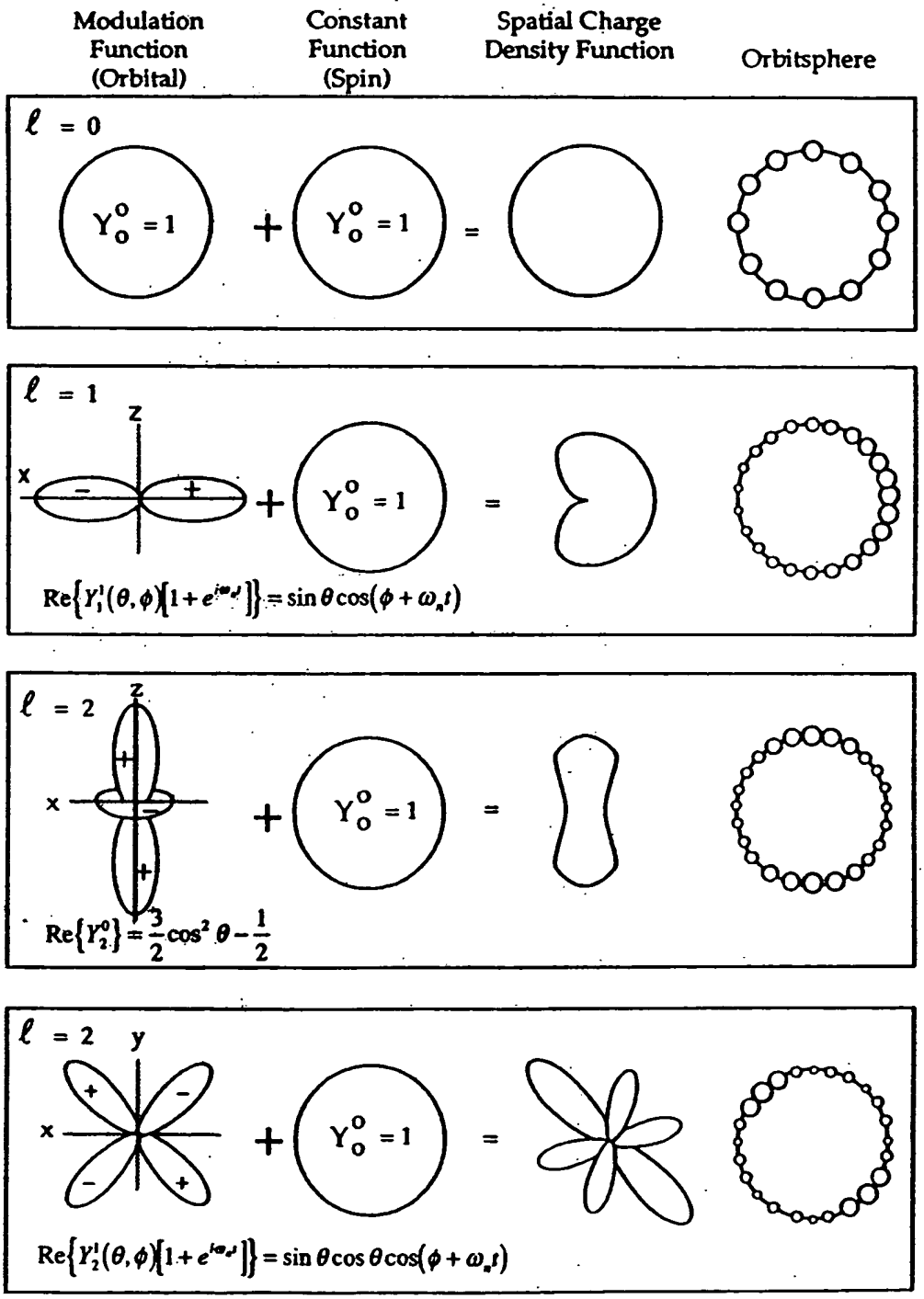
Modulation Function (Orbital)
Constant Function (Spin)
Spatial Charge Density Function
Orbitsphere
ℓ = 0
$Y_0^0 = 1$
+
$Y_0^0 = 1$
=
ℓ = 1
z
x
−
+
+
$Y_0^0 = 1$
=
$\mathrm{Re}\{Y_1^1(\theta,\phi)[1+e^{i\omega_s t}]\} = \sin\theta\cos(\phi+\omega_s t)$
ℓ = 2
z
x
+
−
+
+
$Y_0^0 = 1$
=
$\mathrm{Re}\{Y_2^0\} = \frac{3}{2}\cos^2\theta - \frac{1}{2}$
ℓ = 2
y
x
+
−
−
+
+
$Y_0^0 = 1$
=
$\mathrm{Re}\{Y_2^1(\theta,\phi)[1+e^{i\omega_s t}]\} = \sin\theta\cos\theta\cos(\phi+\omega_s t)$

Fig. 4

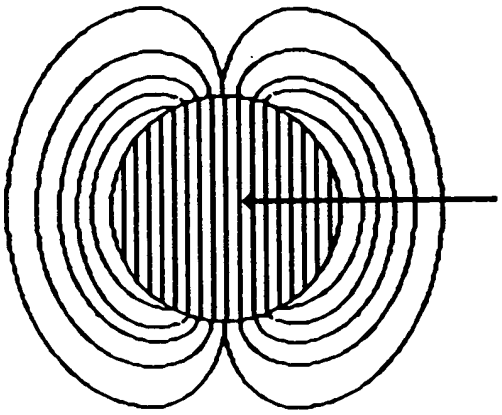

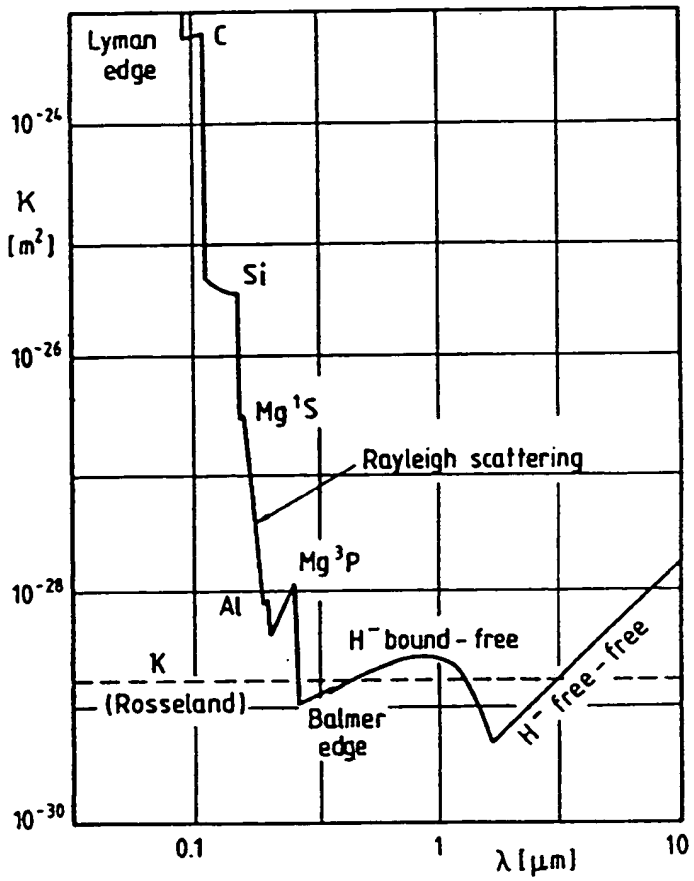
Lyman edge
C
Si
Mg 1S
Rayleigh scattering
Mg 3P
Al
H⁻ bound - free
H⁻ free - free
K
(Rosseland)
Balmer edge
10⁻²⁴
K [m²]
10⁻²⁶
10⁻²⁸
10⁻³⁰
0.1
1
10
λ [μm]

Fig. 5

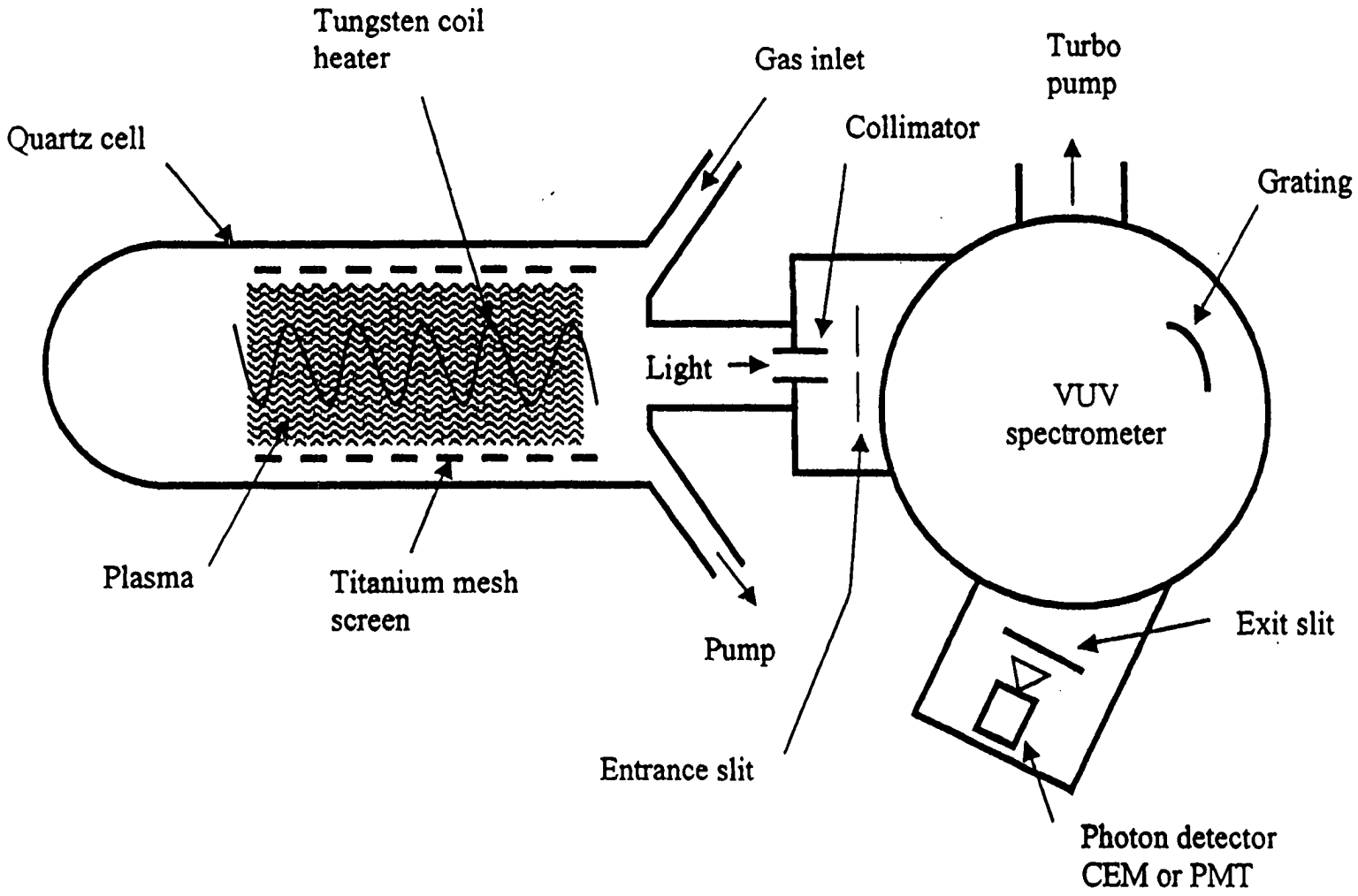
Tungsten coil heater
Gas inlet
Turbo pump
Quartz cell
Collimator
Grating
Light
VUV spectrometer
Plasma
Titanium mesh screen
Pump
Exit slit
Entrance slit
Photon detector CEM or PMT

Fig. 6

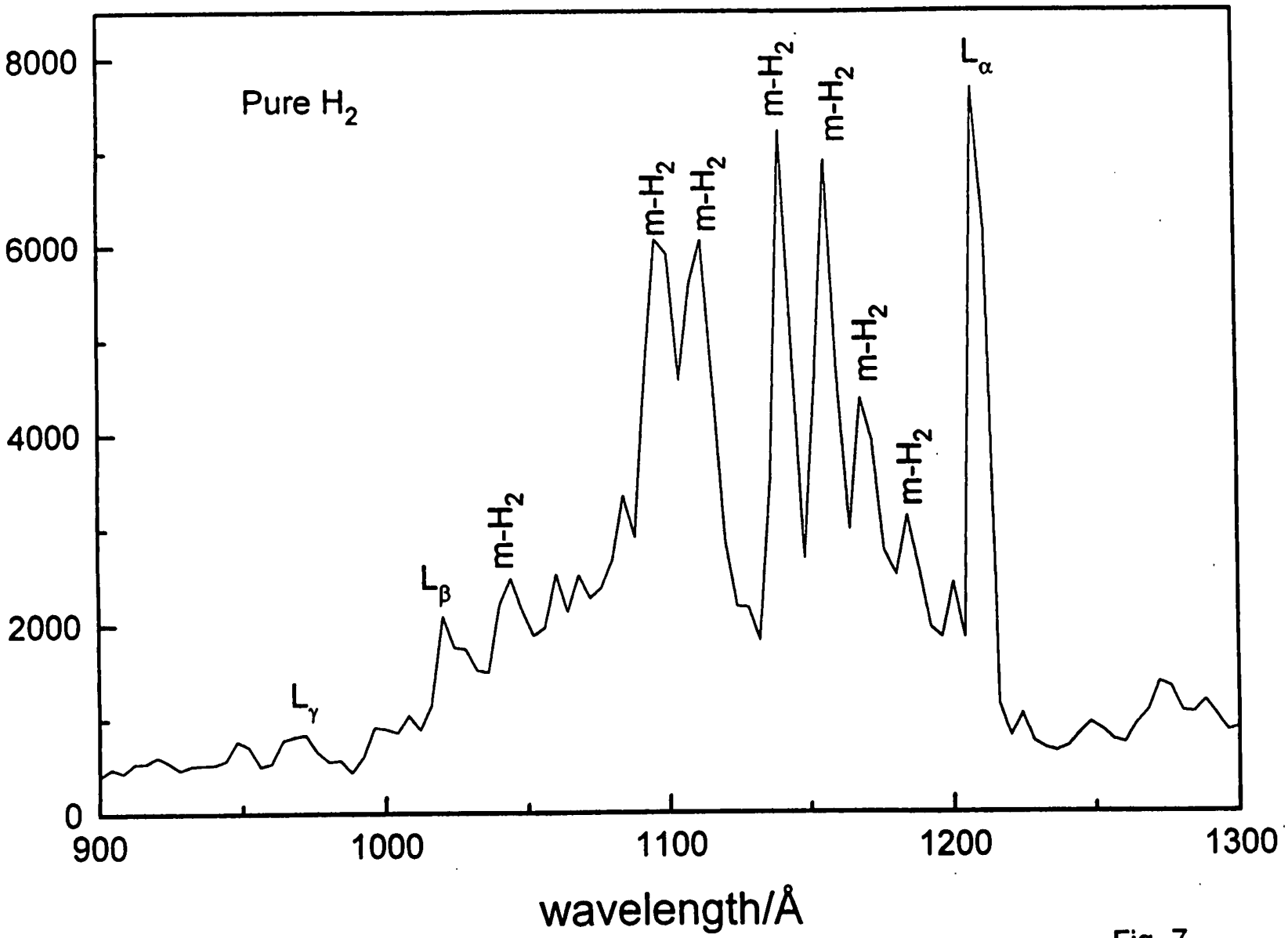
Pure H_2
8000
6000
4000
2000
0
900
1000
1100
1200
1300
wavelength/Å
L_γ
L_β
L_α
m-H_2
m-H_2
m-H_2
m-H_2
m-H_2
m-H_2

Fig. 7

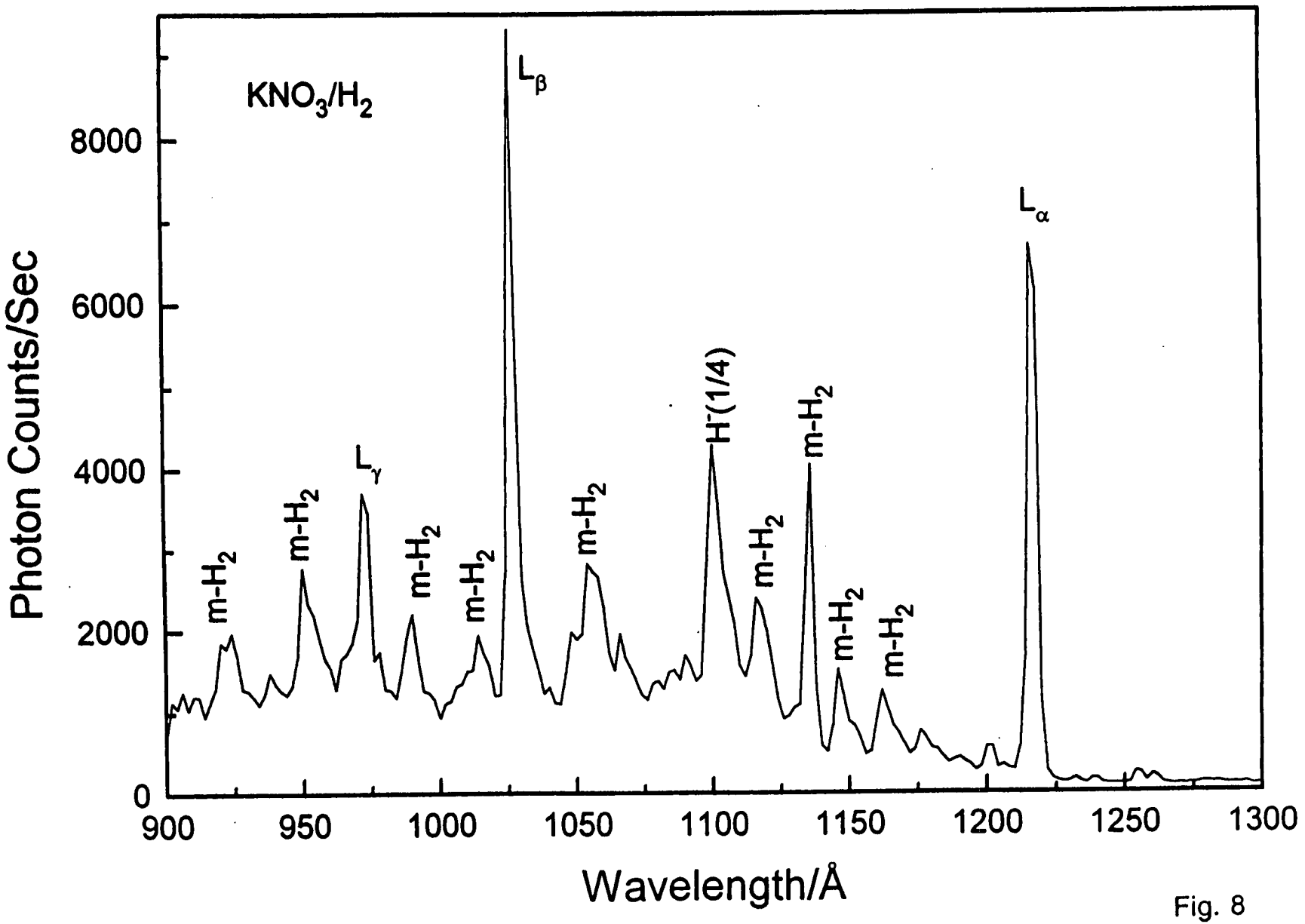
KNO3/H2
Lβ
Lα
Lγ
m-H2
m-H2
m-H2
m-H2
m-H2
m-H2
H-(1/4)
m-H2
m-H2
m-H2
m-H2
Photon Counts/Sec
0
2000
4000
6000
8000
900
950
1000
1050
1100
1150
1200
1250
1300
Wavelength/Å

Fig. 8

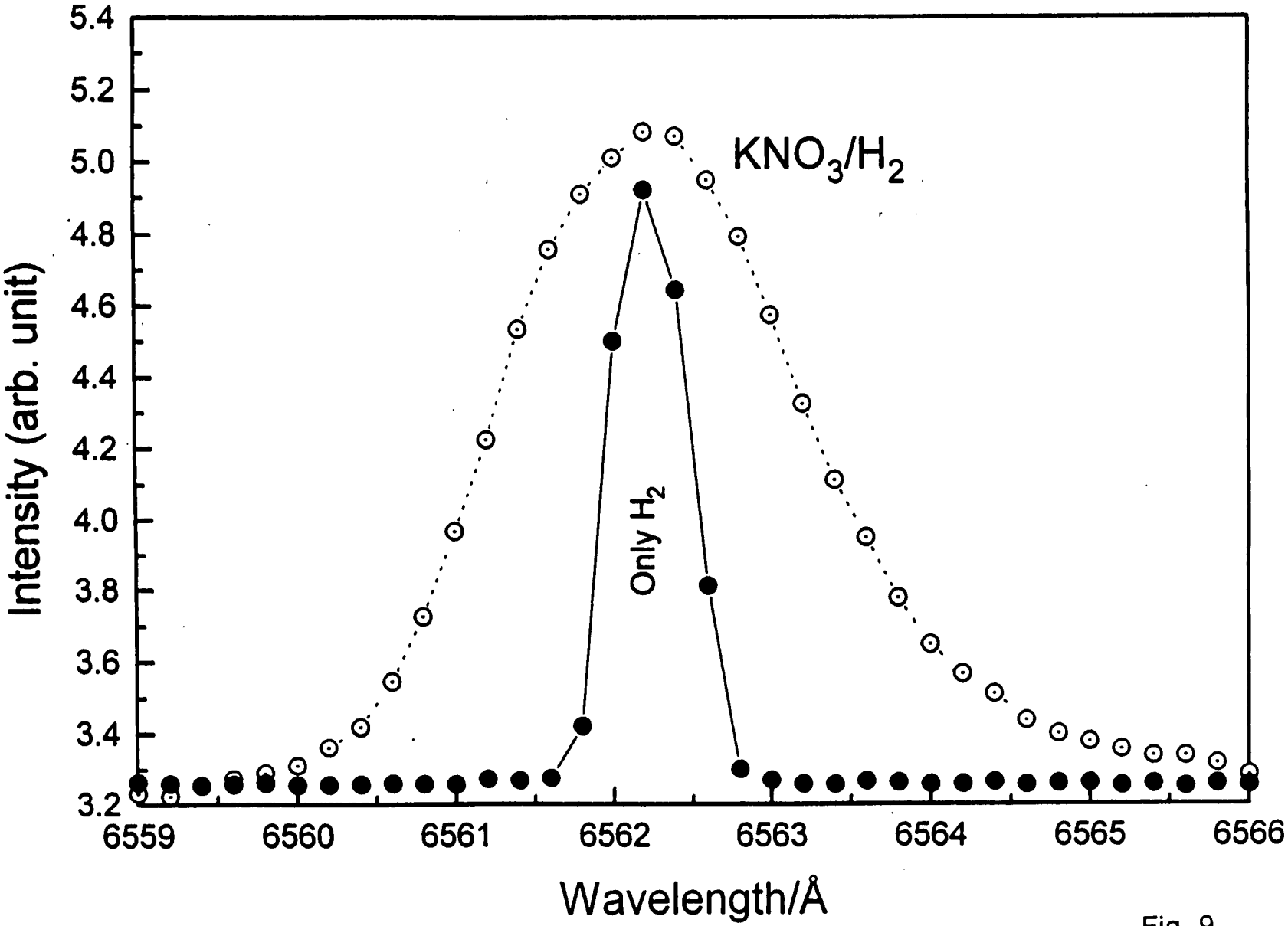
5.4
5.2
5.0
4.8
4.6
4.4
4.2
4.0
3.8
3.6
3.4
3.2
Intensity (arb. unit)
KNO3/H2
Only H2
6559
6560
6561
6562
6563
6564
6565
6566
Wavelength/Å

Fig. 9

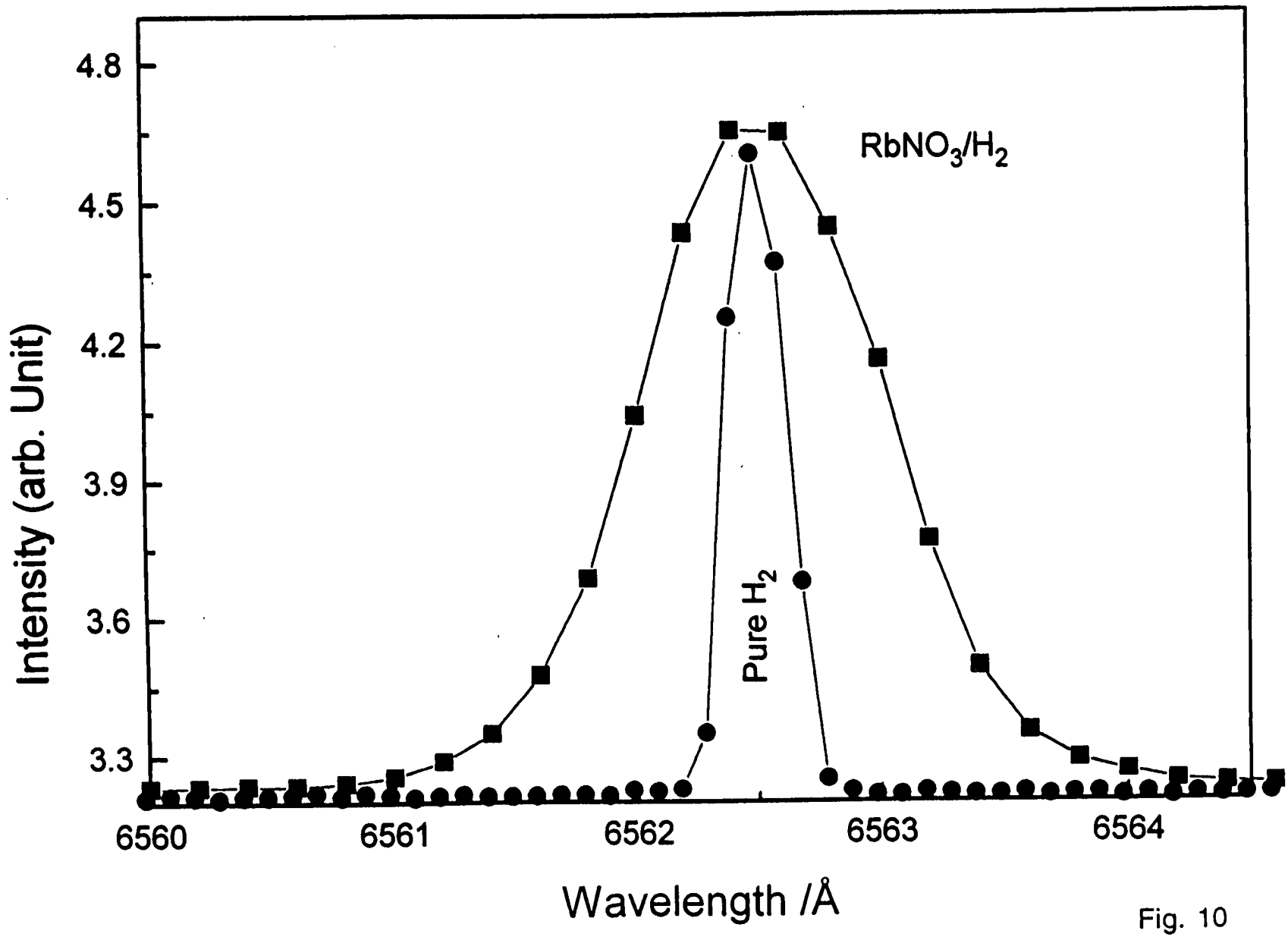
4.8
4.5
4.2
3.9
3.6
3.3
Intensity (arb. Unit)
RbNO3/H2
Pure H2
6560
6561
6562
6563
6564
Wavelength /Å

Fig. 10

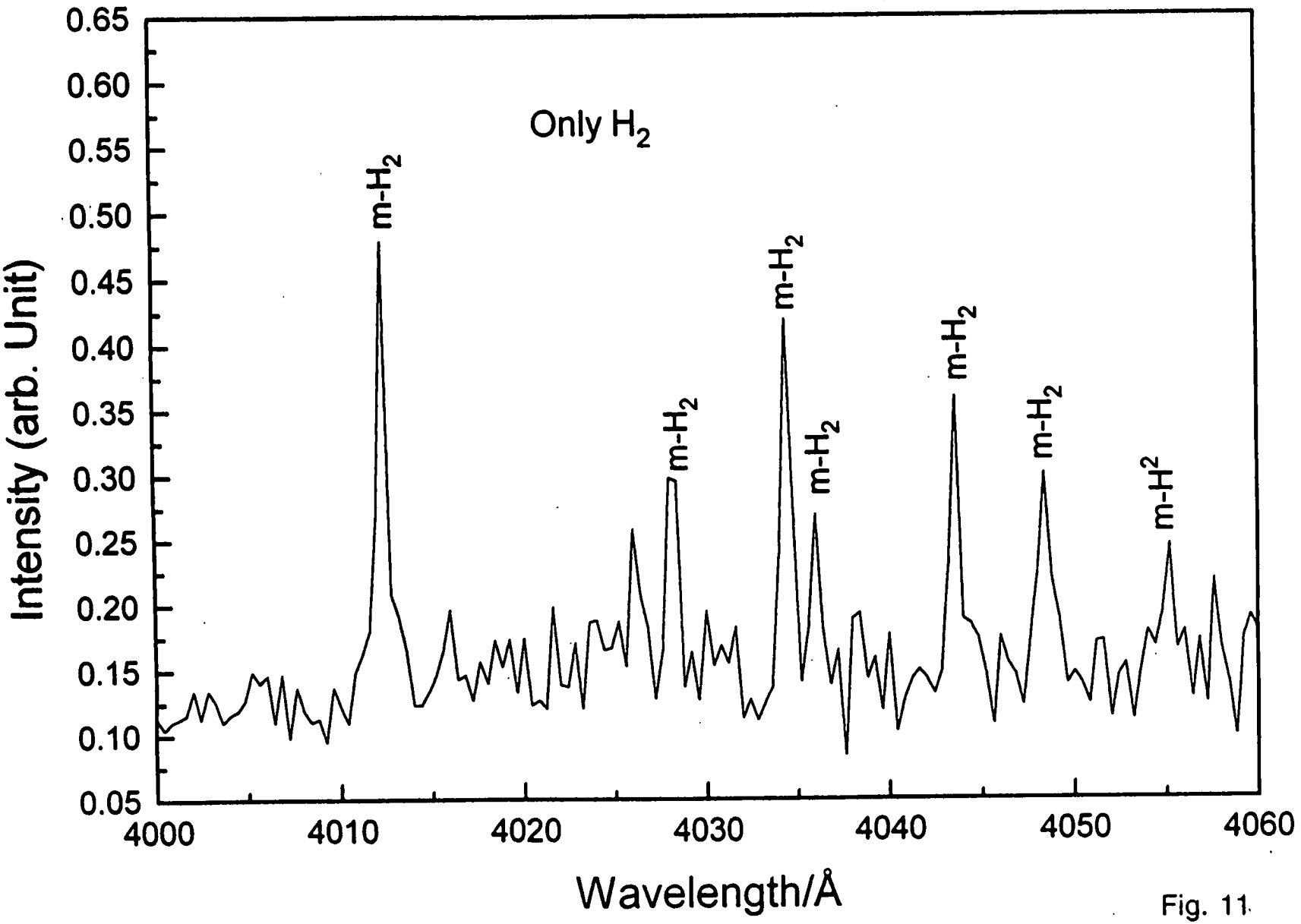
Only H_2
m-H_2
m-H_2
m-H_2
m-H_2
m-H_2
m-H_2
m-H^2
Intensity (arb. Unit)
Wavelength/Å
0.65
0.60
0.55
0.50
0.45
0.40
0.35
0.30
0.25
0.20
0.15
0.10
0.05
4000
4010
4020
4030
4040
4050
4060

Fig. 11

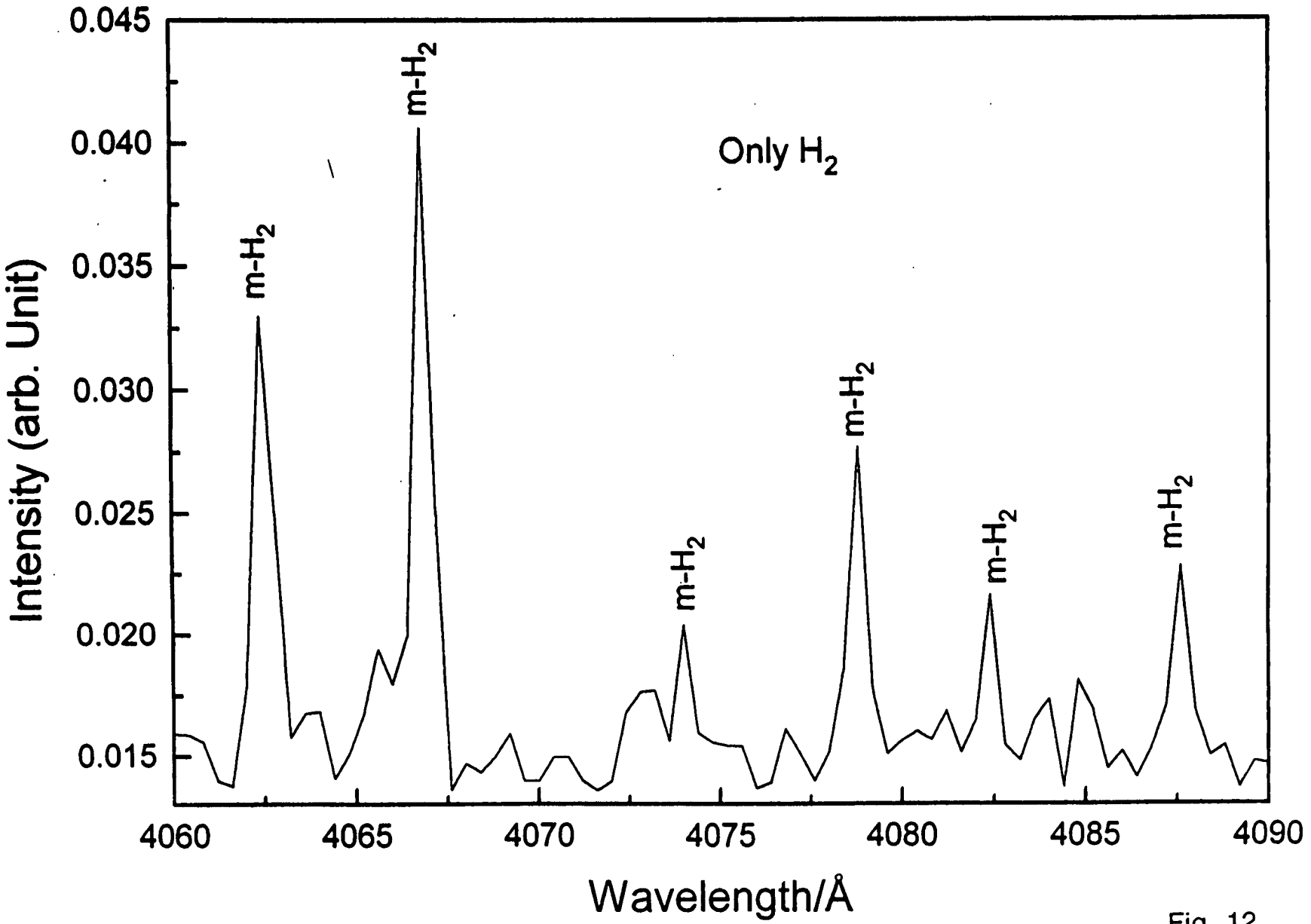
Only H_2
m-H_2
m-H_2
m-H_2
m-H_2
m-H_2
m-H_2
Intensity (arb. Unit)
0.045
0.040
0.035
0.030
0.025
0.020
0.015
4060
4065
4070
4075
4080
4085
4090
Wavelength/Å

Fig. 12

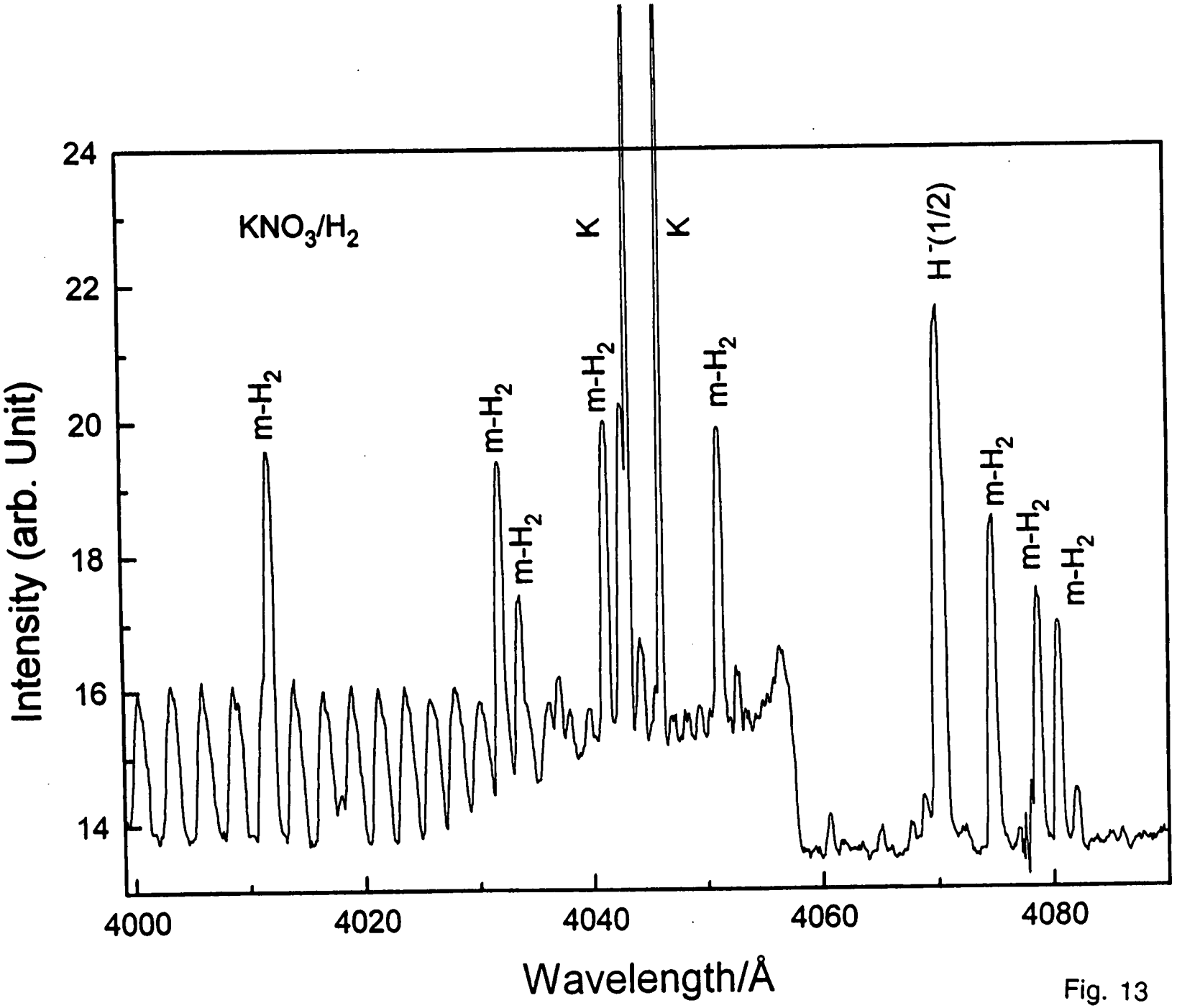
KNO3/H2
K
K
H-(1/2)
m-H2
m-H2
m-H2
m-H2
m-H2
m-H2
m-H2
Intensity (arb. Unit)
24
22
20
18
16
14
4000
4020
4040
4060
4080
Wavelength/Å

Fig. 13

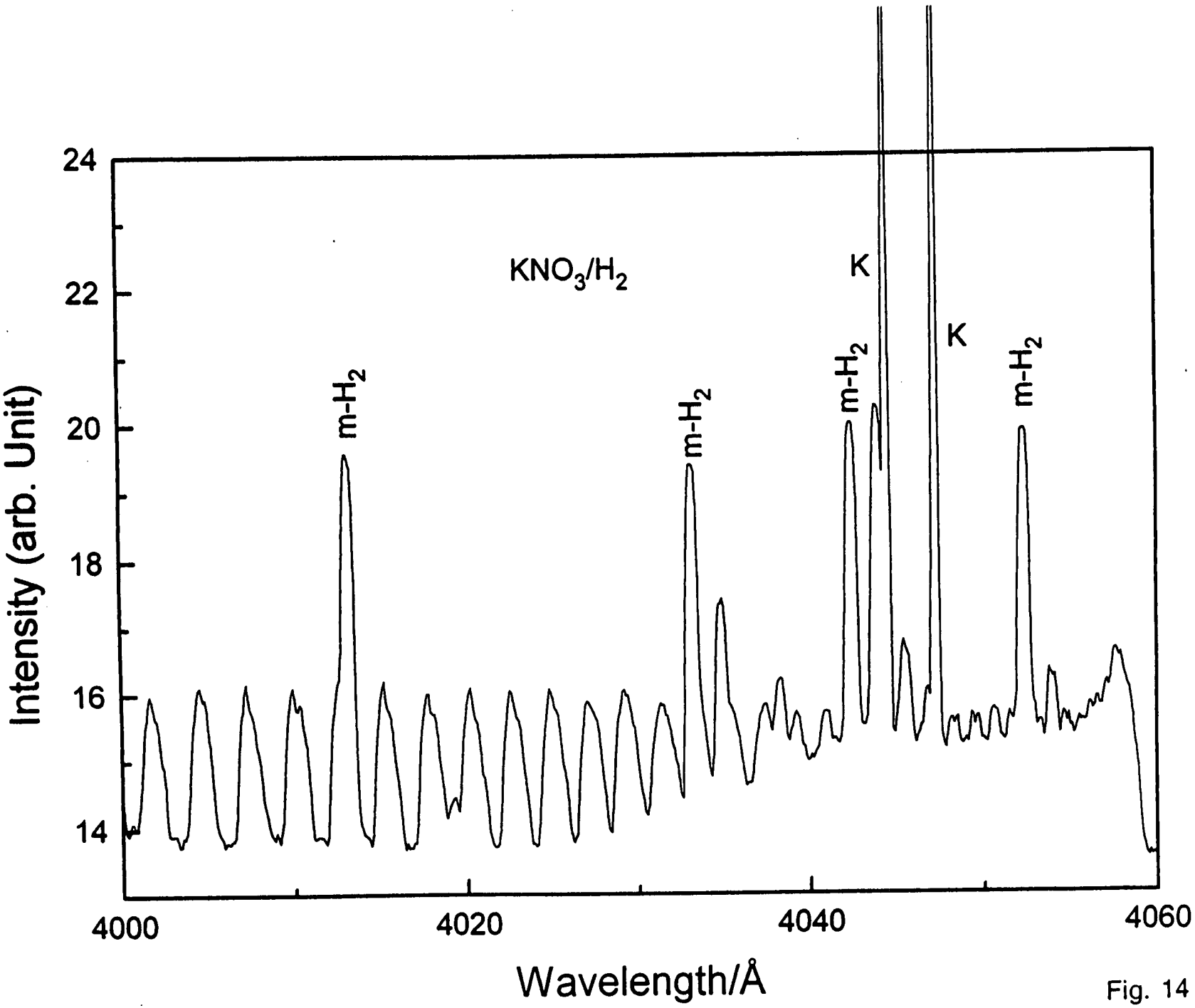
24
22
20
18
16
14
Intensity (arb. Unit)
KNO3/H2
m-H2
m-H2
m-H2
K
K
m-H2
4000
4020
4040
4060
Wavelength/Å

Fig. 14

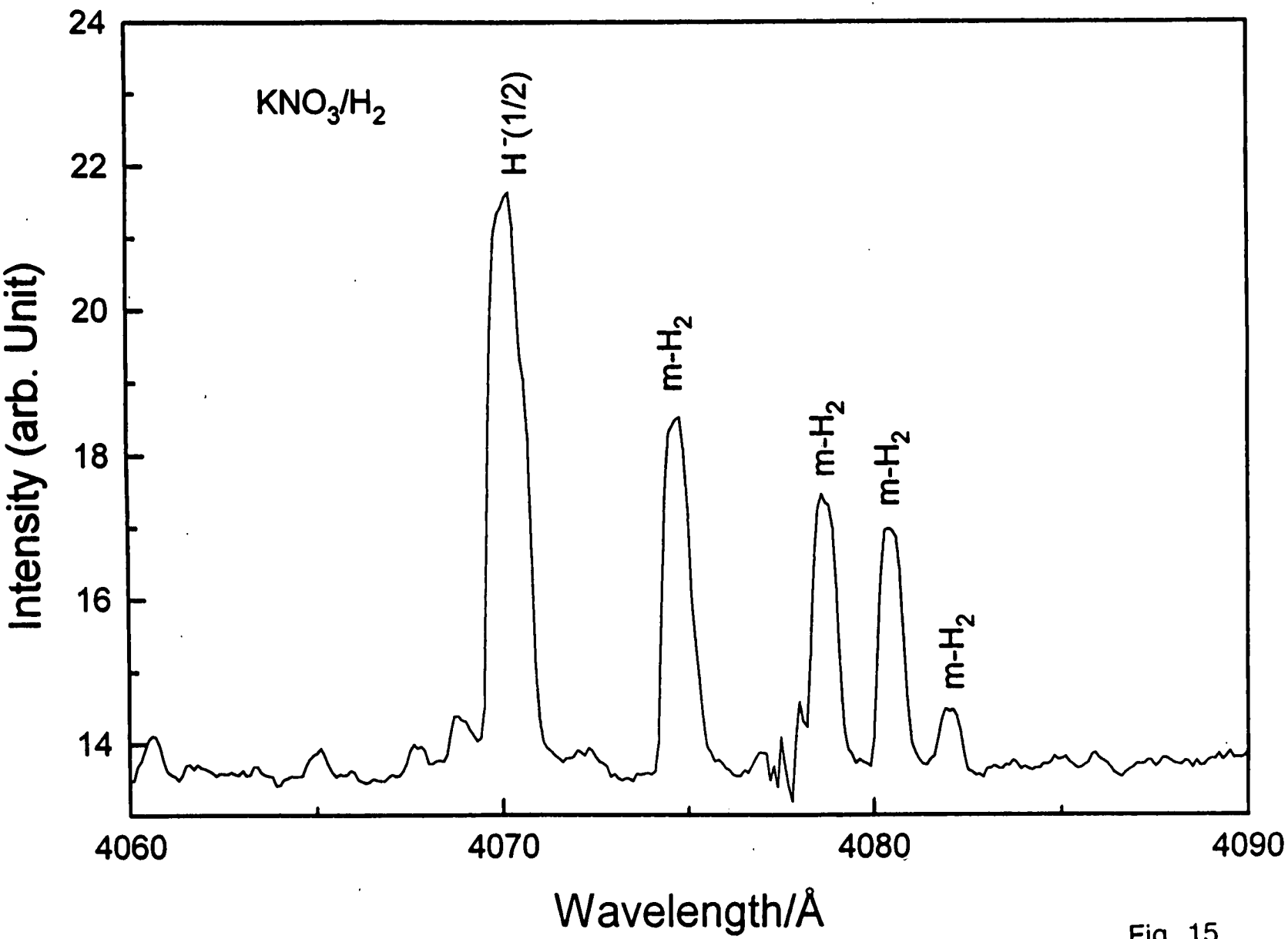
KNO3/H2
H-(1/2)
m-H2
m-H2
m-H2
m-H2
Intensity (arb. Unit)
24
22
20
18
16
14
4060
4070
4080
4090
Wavelength/Å

Fig. 15

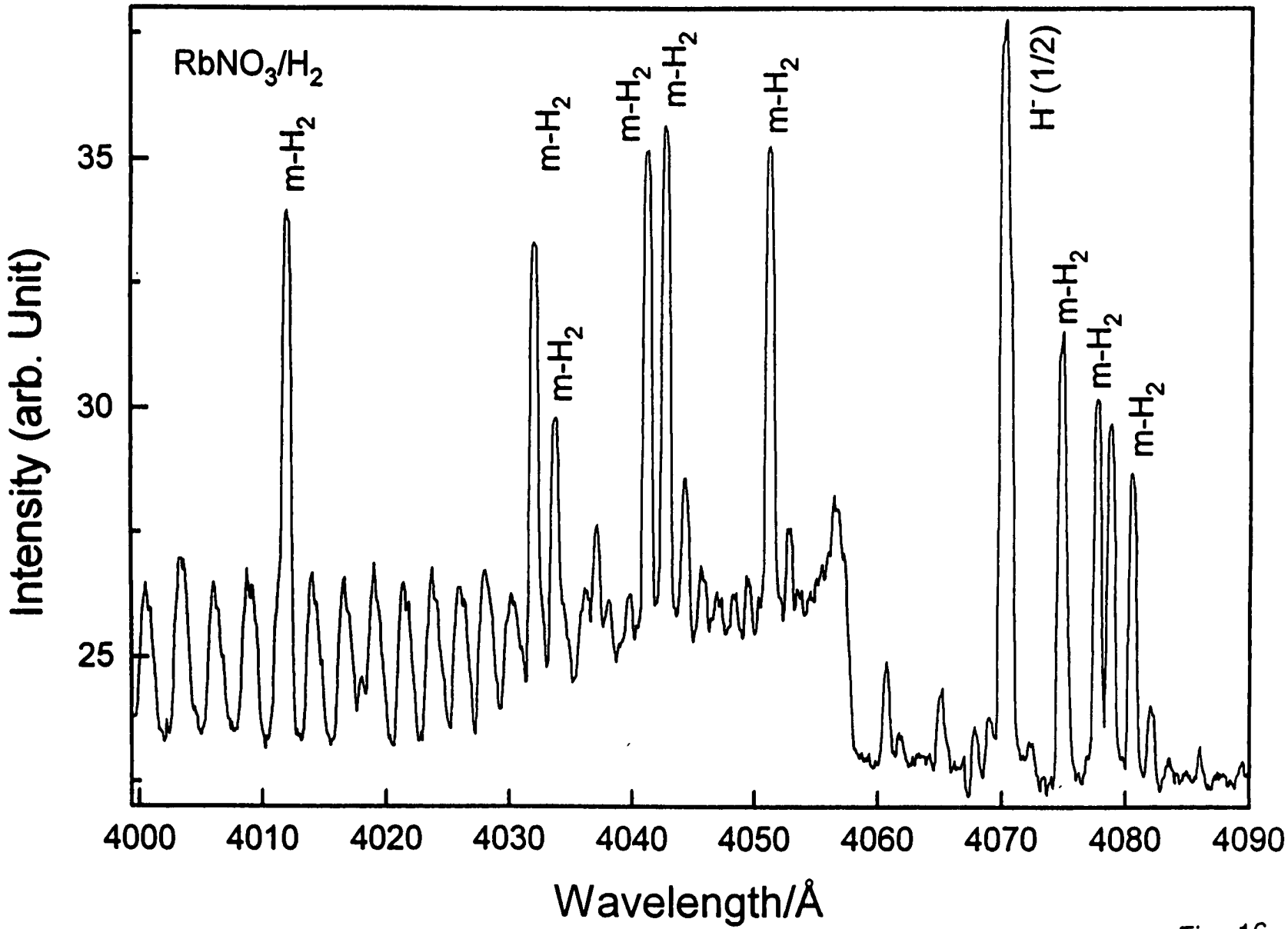
RbNO3/H2
m-H2
m-H2
m-H2
m-H2
m-H2
H- (1/2)
m-H2
m-H2
m-H2
Intensity (arb. Unit)
35
30
25
4000
4010
4020
4030
4040
4050
4060
4070
4080
4090
Wavelength/Å

Fig. 16

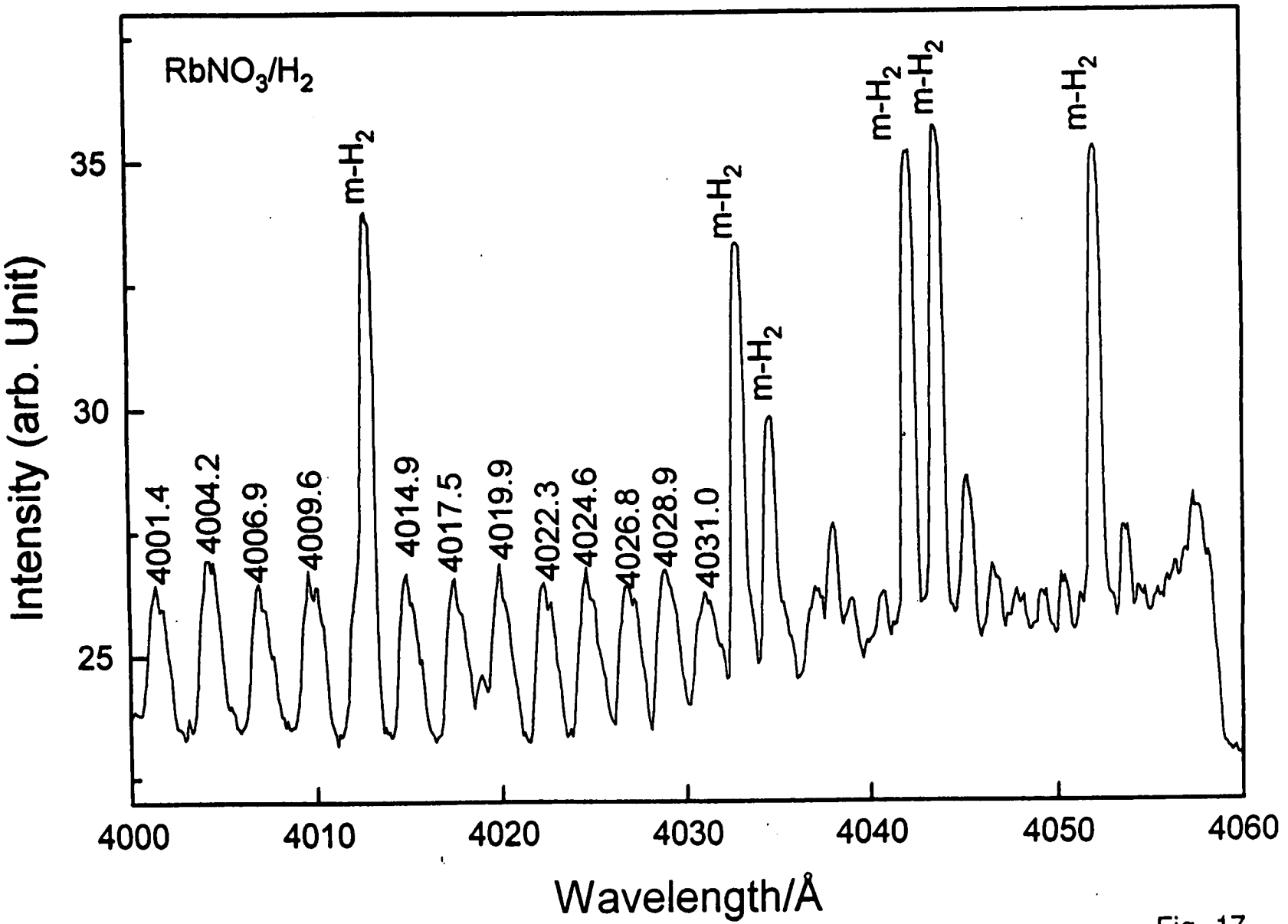
RbNO3/H2
Intensity (arb. Unit)
35
30
25
4000
4010
4020
4030
4040
4050
4060
Wavelength/Å
4001.4
4004.2
4006.9
4009.6
4014.9
4017.5
4019.9
4022.3
4024.6
4026.8
4028.9
4031.0
m-H2
m-H2
m-H2
m-H2
m-H2
m-H2

Fig. 17

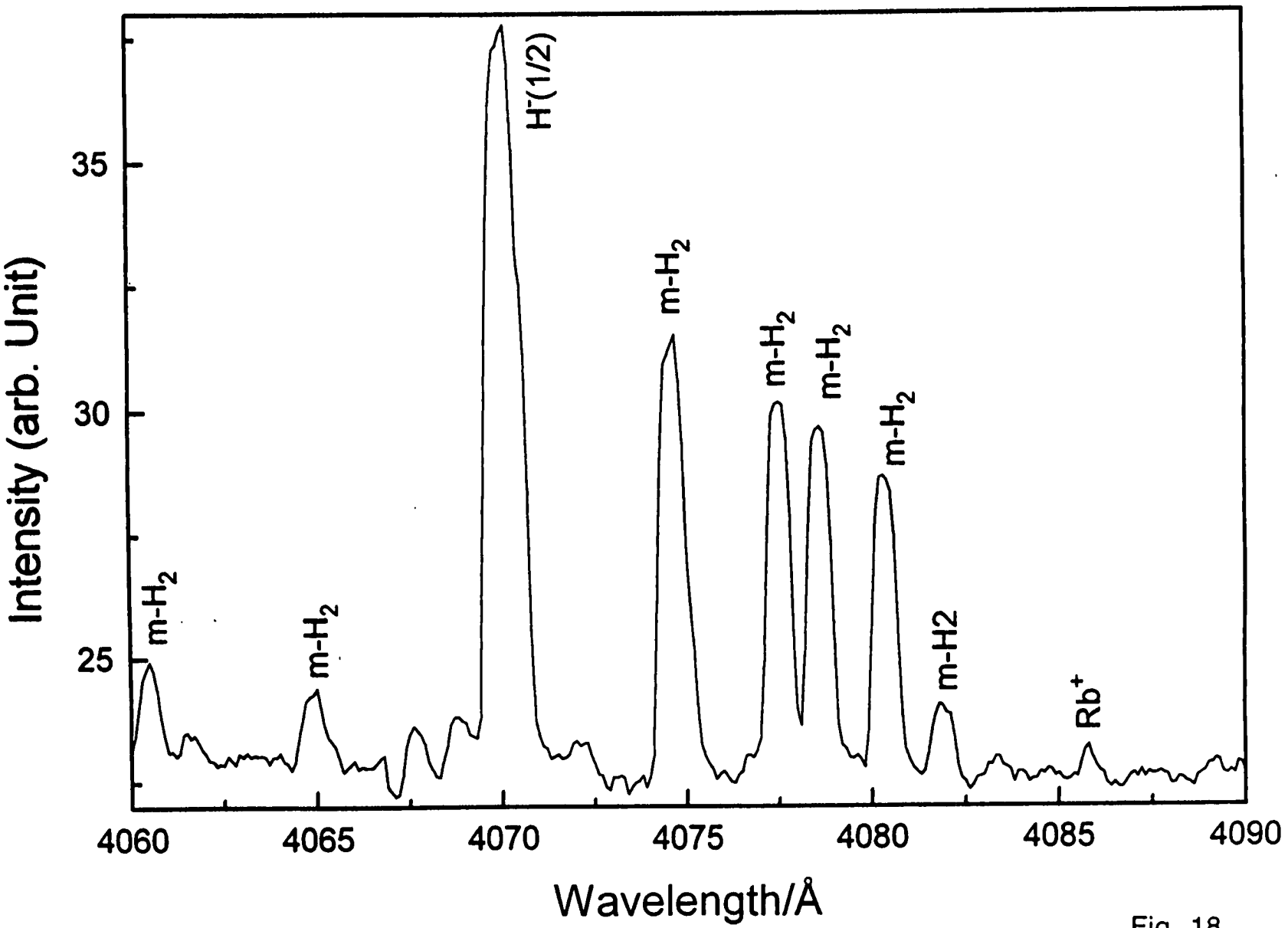
Intensity (arb. Unit)
35
30
25
m-H2
m-H2
H-(1/2)
m-H2
m-H2
m-H2
m-H2
m-H2
Rb+
4060
4065
4070
4075
4080
4085
4090
Wavelength/Å

Fig. 18

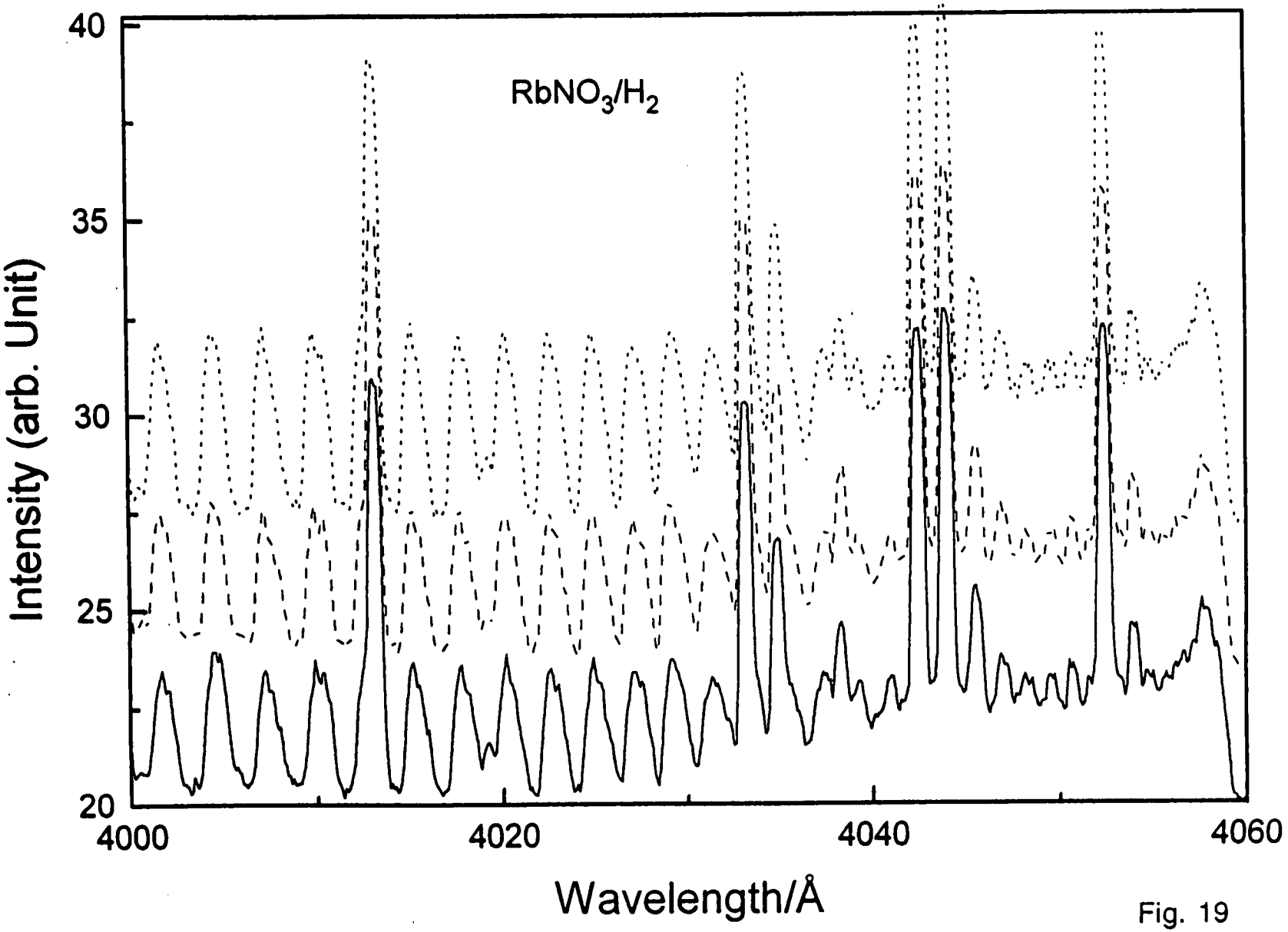
RbNO3/H2
Intensity (arb. Unit)
40
35
30
25
20
4000
4020
4040
4060
Wavelength/Å

Fig. 19

Figure 20

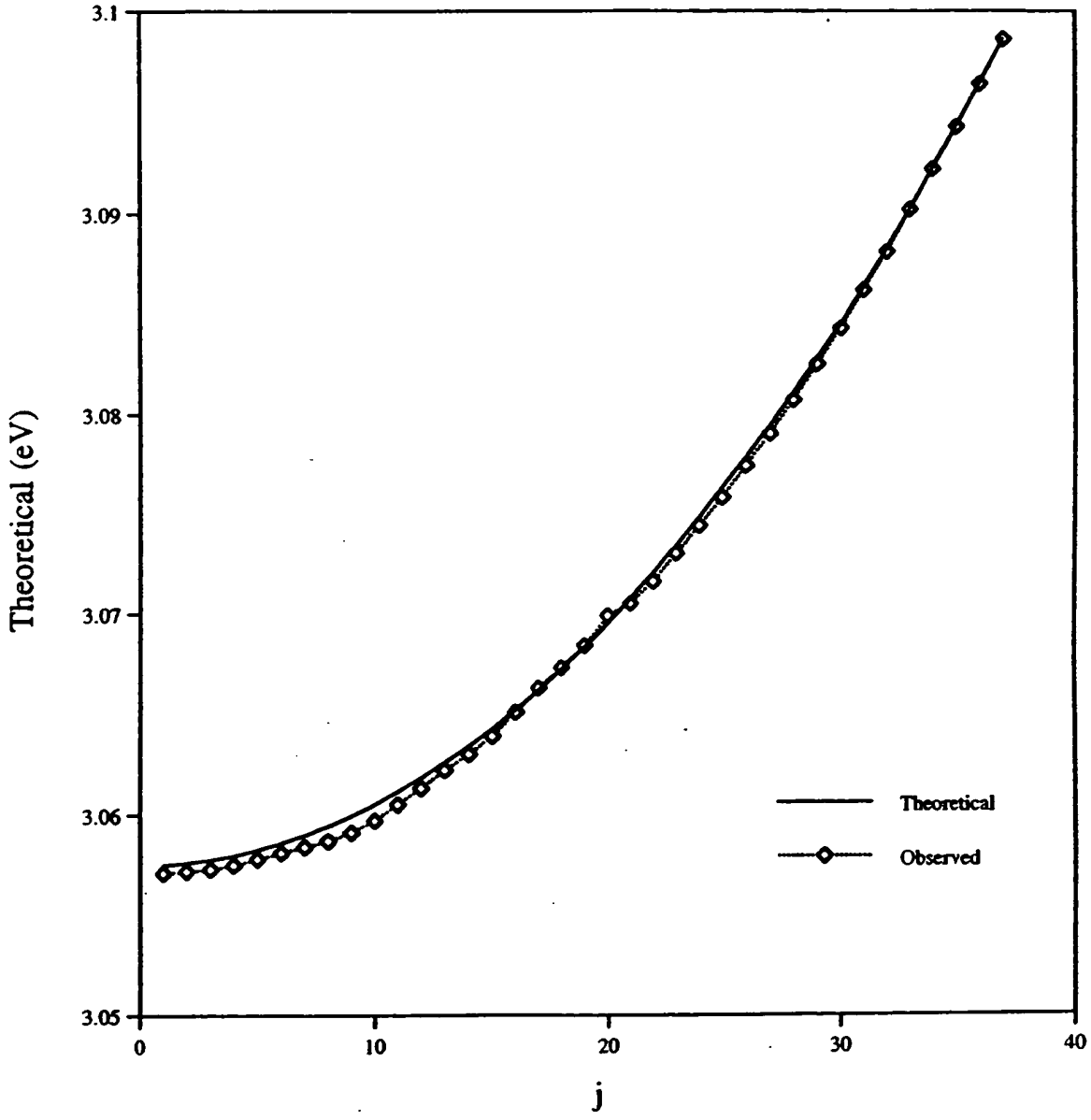
3.1
3.09
3.08
3.07
3.06
3.05
Theoretical (eV)
0
10
20
30
40
j
Theoretical
Observed

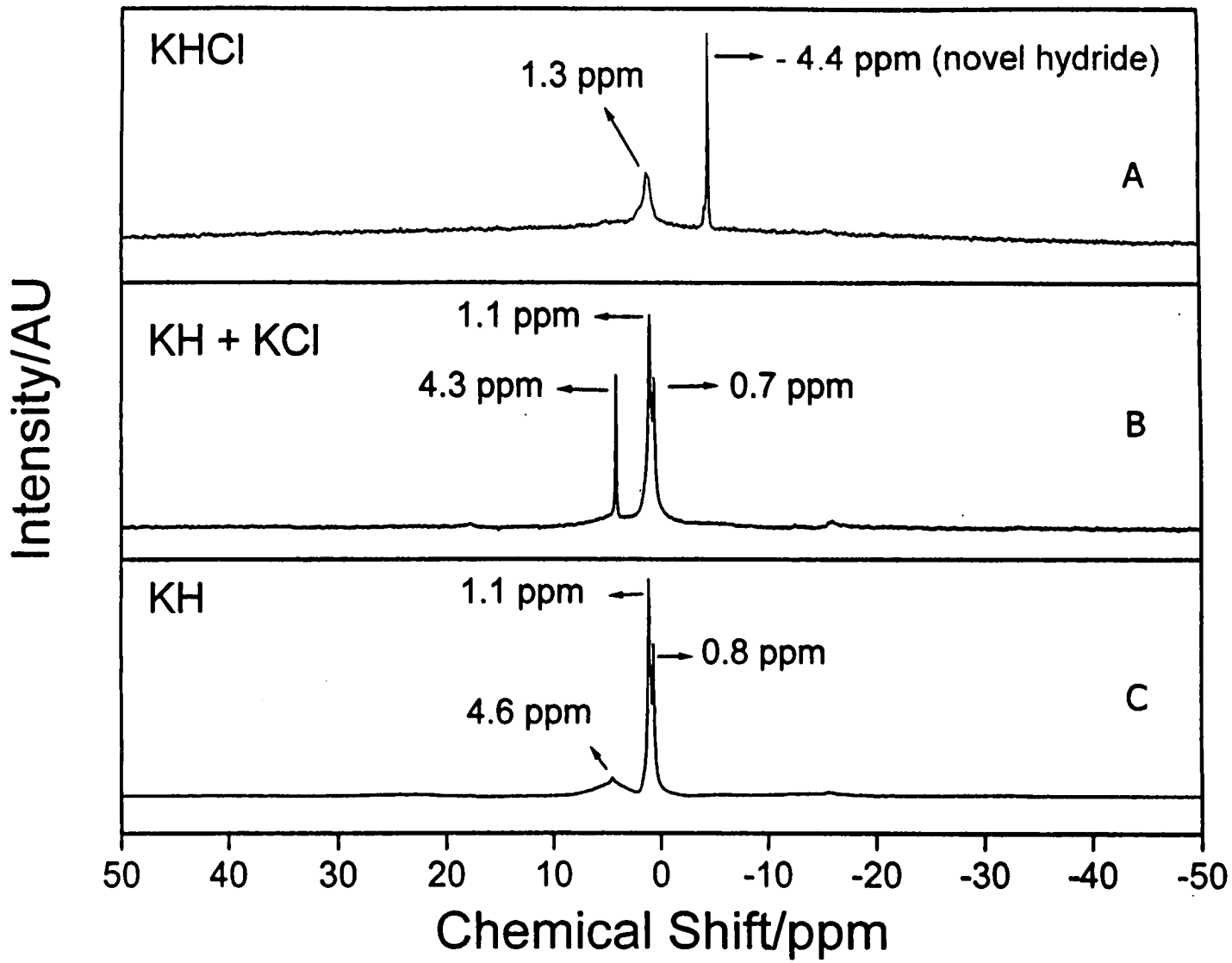
KHCl
1.3 ppm
- 4.4 ppm (novel hydride)
A
KH + KCl
1.1 ppm
4.3 ppm
0.7 ppm
B
KH
1.1 ppm
0.8 ppm
4.6 ppm
C
Intensity/AU
50
40
30
20
10
0
-10
-20
-30
-40
-50
Chemical Shift/ppm

Fig. 21